J. Fluid Mech. (2010), *vol.* 643, *pp.* 59–95.
doi:10.1017/S0022112009991856

Quantitative planar imaging of turbulent buoyant jet mixing

L. K. SU†, D. B. HELMER‡ AND C. J. BROWNELL¶

Applied Fluid Imaging Laboratory, Department of Mechanical Engineering, Johns Hopkins University, Baltimore, MD 21218, USA

(Received 2 September 2008; revised 1 September 2009; accepted 1 September 2009; first published online 9 December 2009)

Planar Rayleigh scattering provides quantitative mixing measurements in the developing region of axisymmetric turbulent helium jets issuing into air. The measurements focus on the relatively near field, in which the jets are primarily momentum driven. The imaging parameters are specified to ensure high spatial resolution. The mean jet fluid concentration fields attain self-similarity within the measurement region, though the forms of the mole fraction profiles indicate a reduction in turbulent transport at the jet outer boundary, arising from the reduced jet fluid density. Nevertheless, jet-like scaling pertains for the concentration fields. Mass fraction fluctuations on the jet centreline attain the expected asymptotic value of $\approx$23 % of the centreline mass fraction values. The scalar dissipation rates, however, show an axial decay rate that is slower than theoretical predictions. The two-dimensional extent of the measurements also allows spatial filtering similar to that inherent in large-eddy simulations (LESs). The results confirm that fluctuation levels and scalar dissipation rates determined for the filtered fields are reduced as the effective resolution is reduced, but while the fluctuation profiles for the filtered fields are similar for the different filter sizes, the forms of the scalar dissipation profiles are highly dependent on filter size. These latter results in particular are of a form that will be useful for grid-dependent assessments of LES results.

Key words: turbulent mixing, turbulent reacting flows, wakes/jets

1. Introduction

There has been long-standing interest in the axisymmetric turbulent jet, arising both because of its direct importance in a variety of engineering applications and because of its value as a well-defined, canonical turbulent shear flow that can offer insight into basic aspects of turbulent flows and more complex shear flow systems. Many applications of the turbulent jet, such as non-premixed combustion, fundamentally depend on the mixing of the jet and ambient fluids. Challenges confronting computational efforts in non-premixed turbulent jet flames include the representation of the effect of significant local fluid density variations on the mixing field and accurate simulation of the properties of the scalar gradient terms, which are important in models for reacting flows. Validation of computations that invoke length-scale

† Email address for correspondence: lsu@jhu.edu
‡ Present address: Mechanical Engineering Department, Stanford University, Stanford, CA 94305, USA
¶ Present address: Department of Mechanical Engineering, United States Naval Academy, Annapolis, MD, 21402, USA

relations, such as large-eddy simulations (LESs), also requires information on mixing-field properties at different levels of resolution. Prior work in axisymmetric turbulent jet mixing by e.g. Becker, Hottel & Williams (1967), Birch *et al.* (1978), George (1989), Dowling & Dimotakis (1990) and Mi, Nobes & Nathan (2001) has explored the properties of the mean jet fluid concentration field, including its turbulent fluctuations and similarity properties. To study variable-density effects, a simple system is the isothermal jet in which jet fluid of one density issues into ambient fluid of a different density. Pitts (1991*a*,*b*) and Richards & Pitts (1993) applied pointwise Rayleigh scattering to study mixing in axisymmetric turbulent jets for different combinations of jet and ambient fluids, with jet–ambient density ratios ranging from 0.14 to 5.11. Panchapakesan & Lumley (1993) studied mixing in the far field of helium jets issuing into air, using hot-wire probes for simultaneous point measurements of velocity and helium concentration in the intermediate region between the jet near field, where the flow is momentum driven, and the far field, which is plume-like.

In the present work, we apply quantitative Rayleigh scattering imaging to a helium jet in air, with a jet-to-ambient fluid density ratio of 0.14. The imaging resolution is designed to allow the accurate measurement of the in-plane spatial gradient components. The data can also be spatially filtered to represent the properties of LES data at the computational grid or filter scales. For non-premixed reacting jets, the mixing in the flow near field has a defining effect on the flame properties, even for lifted flames in which the reaction zones begin downstream from the nozzle (Su, Sun & Mungal 2006). The present imaging measurements extend from just outside the jet exit, allowing the investigation of the axial evolution and similarity properties of the mixing field in regions in which, while buoyancy effects are small, density variations as high as 7:1 reflect typical temperature variations in hydrocarbon–air flames.

Mixing in variable-density jets can be quantified by the local mole fraction X, which measures the proportion by volume of fluid at a given point that originated in the jet, or by the local mass fraction Y, which measures the proportion by mass of jet fluid at a given point. A common method to assess flow development in axisymmetric jets considers the axial evolution of concentration fluctuation magnitudes on the centreline, normalized by the mean centreline concentration values. Sufficiently far from the jet exit, the self-similarity of the turbulent field is presumed to lead to an asymptotic value of the normalized centreline concentration fluctuations. Dowling & Dimotakis (1990) found that the normalized fluctuations in uniform-density jets reached an asymptotic value of $\approx 23\,\%$ as early as 20 diameters from the jet exit. A particularly noteworthy observation by Pitts (1991*a*) is that in variable-density jets, the normalized mole fraction fluctuations on the centreline approach asymptotic values that are dependent on the jet–ambient fluid density ratio, while the normalized mass fraction fluctuations approach the same value of $\approx 23\,\%$. Here we investigate the discrepancies between the present mole fraction and fluctuation results and the results from constant-density jets, to attempt to identify the particular mechanisms from which the density dependence arises.

It is often useful to investigate mixing in terms of the scalar dissipation rate χ, which is commonly defined as the loss term in the evolution equation for the square of a scalar quantity (e.g. Y). For flows with variable density ρ (but with constant diffusivity D_Y between the jet and ambient fluids), this evolution equation is given by

$$\frac{\partial(Y^2)}{\partial t} + \boldsymbol{u}\cdot\nabla(Y^2) - D_Y\nabla^2(Y^2) - \frac{D_Y}{\rho}\nabla\rho\cdot\nabla(Y^2) = -2D_Y\nabla Y\cdot\nabla Y \equiv \chi. \tag{1.1}$$

(Other definitions of χ, based on the evolution equation for $Y^2/2$ or for the scalar fluctuations Y', do not have significant qualitative differences from this definition.) For non-premixed combustion, for example, χ (normalized by Y'_{rms}) is interpreted as the inverse of the mixing time scale that is established by the flow field. Under fast chemistry conditions χ is directly proportional to the instantaneous volumetric reaction rate (Bilger 1976*a*,*b*). Properties such as flame stabilization and extinction also depend on χ. The definition of χ in terms of spatial gradients means that its measurement by conventional single-point methods requires multiple measurement probes (Lockwood & Moneib 1980; Effelsberg & Peters 1988). However, reported measurements have been unable to reproduce theoretical predictions for the axial evolution of χ on the centreline of axisymmetric turbulent jets (Peters & Williams 1983; Bilger 2004). The present planar measurements inherently allow spatial differentiation in both in-plane directions, which, together with the assumption of axial symmetry, allows the direct measurement of χ on the jet centreline. Ensuring that the grid spacing of the imaging planes is sufficiently small to resolve the fine dissipation scales, however, means that the imaging planes must be reasonably small. Partly for this reason, prior planar measurements of χ (e.g. Buch & Dahm 1996, 1998; Su & Clemens 1999, 2003) have generally focused on small-scale mixing properties; in addition, Bilger (2004) has argued that the spatial resolution requirements for measuring scalar dissipation rates from planar imaging data have not been well explored. In the present work, we seek to maintain spatial resolution sufficient for measuring the scalar gradients by dividing the full measurement domain into a series of five smaller sub-windows. Each sub-window spans the order of the local jet width while resolving the characteristic length scales of the scalar gradient terms.

The spatial extent of the planar measurements makes the results ideal for assessments of LESs of jet mixing. LES of round jets has been reported by Olsson & Fuchs (1996), Basu & Mansour (1999), Boersma (2004) and Suto *et al.* (2004). LES results are, by definition, grid dependent, meaning that computed quantities such as scalar fluctuations and gradients will depend on the resolution of the grid (or filter) scale used for the simulations. Fully resolved experimental data, or direct numerical simulation (DNS) results, are thus inappropriate for assessing LES results for grid-scale fluctuations and gradients. In this work we will investigate the issue of grid dependence by applying two-dimensional filters of different sizes to the planar measurements and then considering the similarity properties and axial evolution of the fluctuations and gradients computed on the filtered results. The grid dependence of the scalar fluctuations is particularly interesting: it has been long recognized (Leonard 1979; Zalesak 1979) that computations of the transport equation for a passive scalar can incur numerical instabilities that must be artificially controlled; so accurate representation of scalar fluctuations is especially challenging, even without grid dependence effects.

The first primary objective of the present work is to demonstrate the use of Rayleigh scattering imaging to make quantitative measurements of mixing, with high spatial resolution, in the buoyant helium–air jet. Section 2 presents details of the imaging arrangement and data reduction procedure, including a novel method for measuring background light levels. We then apply those measurement results to investigate the similarity and scaling properties of the mixing field, including the values of the mean scalar, scalar fluctuations and scalar dissipation rate in the developing region of the flow (§ 3.2–§ 3.4). Finally, we consider the effect of LES-type spatial filtering on the measured fluctuations and dissipation rates in § 3.6.

u_0	Re_0	$x_{Fr,max}$	x_j	θ	x_{max}/θ	Re_δ
21.7 ms^{-1}	800	1.54	12.4d	7.9d	4.8	5400
40.1 ms^{-1}	1500	0.83	22.8d	14.7d	2.6	10 100
66.5 ms^{-1}	2500	0.50	37.9d	24.6d	1.5	16 800

TABLE 1. Flow conditions for the buoyant jet experiments (quantities defined in § 2.1).

2. Experimental method

2.1. *Run conditions*

In these experiments a helium jet flow issues vertically upward from a nozzle with inner diameter $d = 4.6$ mm and length $44d$. The jet is surrounded by a slow ($u_\infty = 0.5$ m s^{-1}) co-flow of air. Both the jet and co-flow fluids are passed through high-efficiency particulate-arresting (HEPA) filters to eliminate particulate Mie scattering in the imaging region. Table 1 summarizes the run conditions for the experiments. We consider three jet exit bulk velocities, $u_0 = 21.7$ m s^{-1}, 40.1 m s^{-1} and 66.5 m s^{-1}. At room temperature and pressure, helium has density $\rho_0 = 0.165$ kg m^{-3} and dynamic viscosity $\mu_0 = 2.0 \times 10^{-5}$ kg (m s)$^{-1}$; so the corresponding jet exit Reynolds numbers (determined using the jet exit excess velocities) are, respectively, $Re_0 = 800$, 1500 and 2500. The measurement region extends to $x = 38.04d$ downstream from the jet exit.

A full characterization of the flow system must account for the co-flow velocity, the effects of the positive jet buoyancy and the effects of the different jet and ambient fluid densities apart from buoyancy. While the momentum flux at the jet exit is J_0, the momentum flux at any downstream section (defined by fixed x) increases with downstream distance, as the jet fluid elements are accelerated by buoyancy. In the near field, then, the scaling of the flow, as quantified by the centreline mean velocity and the mean velocity profile width, will evolve similar to pure, momentum-driven jets; after a transitional region, the integrated effect of buoyancy will become dominant in comparison with the initial momentum, and the flow will observe plume-like scaling. Chen & Rodi (1980) quantified the axial ranges of these regimes using a scaled coordinate x_{Fr}, which is defined as

$$x_{Fr} = Fr^{-1/2} \left(\frac{\rho_\infty}{\rho_0} \right)^{1/4} \frac{x}{d}, \tag{2.1}$$

where ρ_∞ is the density of air and $Fr \equiv u_0^2/(gd(\rho_\infty - \rho_0)/\rho_0)$ (g is the gravitational acceleration) is a Froude number based on jet exit conditions. For $x_{Fr} \lesssim 0.5$, the flow is in the momentum-driven, jet-like regime, while for $x_{Fr} \gtrsim 5$, plume-like scaling pertains. Table 1 shows $x_{Fr,max}$, which is x_{Fr} at the downstream limit of the measurement region, as well as x_j, defined as the value of x such that $x_{Fr} = 0.5$, for each of the jet Reynolds numbers. The $Re_0 = 2500$ case is fully momentum driven throughout the measurement regime, while the other cases cross from the momentum-driven regime into the transitional regime at $x \approx 12d$ and $23d$, respectively. Neither of the two lower-Re_0 cases approaches the buoyancy-driven regime.

Results for flow scaling in variable-density momentum-driven jets can be made consistent when the axial coordinate is normalized by an effective jet diameter, defined by Dahm & Dimotakis (1987) as

$$d^* \equiv \frac{2m_0}{(\pi \rho_\infty J_0)^{1/2}} \approx d \left(\frac{\rho_0}{\rho_\infty} \right)^{1/2}, \tag{2.2}$$

where m_0 is the jet exit mass flow rate. The final expression applies the approximation $J_0 \approx (\pi d^2/4)\rho_0 u_0^2$, which is exact only if the velocity profile has a top-hat form; Pitts (1991*a*) pointed out that $d(\rho_0/\rho_\infty)^{1/2}$ is within 5 % of the true d^* even for pipe flow velocity profiles.

The significance of the co-flow to the flow development is quantified in terms of the momentum radius θ, which is defined using the jet excess momentum flux J_0 as

$$\theta \equiv \left[\frac{J_0}{\pi\rho_\infty u_\infty^2}\right]^{1/2} = d\left(\frac{\rho_0}{\rho_\infty}\right)^{1/2}\frac{u_e}{u_\infty}. \tag{2.3}$$

That is θ is the jet radius that would be required for a jet with velocity u_∞ to have momentum flux J_0. For sufficiently small x/θ, the effect of the co-flow is negligible and the flow resembles a pure jet, while for large x/θ, as the jet velocity decays, the co-flow becomes dominant and the flow observes wake scaling. For the three jet exit Reynolds numbers here, the measurement region extends no further than $x/\theta = 4.8$ downstream from the jet exit (table 1). Nickels & Perry (1996) showed that pure jet scaling pertains up to $x/\theta \approx 10$; so the effect of the co-flow on the mean flow development can be neglected in the present measurements.

While the jet exit Reynolds number, defined in terms of the kinematic viscosity of the jet fluid, is familiarly used to characterize and specify jet flows, the wide disparity between the jet and ambient fluid properties in these measurements means that the downstream turbulence level is more precisely described in terms of an outer-scale Re computed in terms of the viscosity of air, which reflects that the entrained air quickly predominates in the flow. Let the mean mass flow rate across fixed-x sections in a jet be $m(x) = m_e(x) + m_0$, where m_0 is the jet exit mass flow rate and $m_e(x)$ is the mass flow rate of entrained fluid at x. Ricou & Spalding (1961) measured these mass flow rates in axisymmetric jets with varying density and found

$$\frac{m_e(x)}{m_0} = 0.32\sqrt{\frac{\rho_\infty}{\rho_0}}\,\frac{x - x_0}{d}. \tag{2.4}$$

The location $x = x_0$ in (2.4) is the effective virtual origin for the mass entrainment, where $m_e = 0$. For these helium–air jets, $\rho_\infty/\rho_0 = 7.24$; so by $x = 10\,d$ the flow consists of 88 % entrained fluid by mass, and by $x = 20\,d$, the flow contains 94 % entrained fluid. Here, we define the outer-scale Reynolds number as $Re_\delta \equiv u_c\delta/\nu_\infty$, where $u_c(x)$ is the mean jet centreline velocity and $\delta(x)$ is the full width of the mean axial velocity profile at 5 % of the centreline velocity. The present work does not include velocity field measurements; so to find u_c and δ we apply the recommended scalings given by Chen & Rodi (1980) for pure jets (neglecting buoyant acceleration):

$$u_c = 6.2\,u_0\sqrt{\frac{\rho_0}{\rho_\infty}}\left(\frac{x}{d}\right)^{-1}, \quad \delta = 0.36\,x. \tag{2.5}$$

Thus Re_δ is uniform for a given axisymmetric jet, and the jet exit Reynolds numbers $Re_0 = 800$, 1500 and 2500 correspond to $Re_\delta = 5400$, 10 100 and 16 800 respectively. Dimotakis (2000) has argued that the so-called mixing transition, beyond which the mixing field attains its asymptotic, high-Reynolds-number state, occurs in jets in the range $Re_\delta = 10000$–20000 (using the present definition of Re_δ). The $Re_0 = 1500$ and 2500 jets here should thus be well representative of high-Reynolds-number mixing.

2.2. *Rayleigh scattering imaging*

Rayleigh scattering, the elastic light scattering from particles with diameter smaller than the incident light wavelength, for example gas molecules (Eckbreth 1988), is

familiar in gas-phase scalar imaging experiments (Escoda & Long 1983; Yip & Long 1986; Buch & Dahm 1998; Su & Clemens 1999, 2003). The Rayleigh scattering cross-section σ of a given species depends on its index of refraction n as $\sigma \propto (n-1)^2$. For a mixture, the scattering cross-section σ_m is the mole-fraction-weighted average of the cross-sections of the constituent species. Under isothermal and isobaric conditions the number density of molecules is constant, and the local (background-corrected) Rayleigh scattering signal level S_R from a mixture can be written as

$$S_R \propto I \cdot E \cdot \sigma_m = I \cdot E \sum_j X_j \sigma_j, \tag{2.6}$$

where I quantifies the local incident (laser) light intensity; E measures both scattering efficiency (which does not vary in these experiments) and signal collection efficiency; and X_j and σ_j are the mole fraction and Rayleigh scattering cross-section, respectively, of species j at the given location. In the present experiments, I and E can be measured at each point, and so we can determine $S_F = S_R/(I \cdot E)$, the fully corrected Rayleigh scattering signal; then, since the mixture consists of two species, namely air and helium, we can invert this corrected scattering signal to find the helium mole fraction X_{He}, uniquely, as

$$X_{He} = \frac{1 - S_R/(I \cdot E)}{1 - \sigma_{He}/\sigma_{air}} \tag{2.7}$$

using $X_{air} + X_{He} = 1$. Details of the data reduction procedure appear in § 2.3.

Most imaging work that uses Rayleigh scattering involves the binary mixing of a relatively high-index gas, such as propane (Buch & Dahm 1998; Su & Clemens 1999, 2003) or Freon (Yip & Long 1986), with air ($n_{air} \approx 1.000292$). Propane has an index of refraction $n_{C_3H_8} \approx 1.001081$ (Bartels *et al.* 1962); so its scattering cross-section is over 13 times that of air. For a propane jet issuing into air, regions with high jet fluid concentration give high scattering signal, while the lowest signal levels correspond to ambient fluid regions. In contrast, for the present helium jets issuing into air, the index of refraction of helium is $n_{He} \approx 1.000035$, and so $\sigma_{He}/\sigma_{air} = 1/72$ in (2.7); thus, regions with high jet fluid concentration give low scattering signal, and the highest signal levels will correspond to the ambient air. We will refer to the diagnostic arrangements with a high- and low-index jet fluid as, respectively, 'positive' and 'negative' scattering. The highest signal levels for the negative scattering experiments will only be equivalent to the lowest signal levels in positive scattering, and the contrast between the highest and lowest signal levels in negative scattering will be much lower than the contrast between extreme values in positive scattering (e.g. $|\sigma_{He} - \sigma_{air}| \approx |\sigma_{C_3H_8} - \sigma_{air}|/13$). Achieving quantitative accuracy in the negative scattering imaging experiments therefore poses particular challenges both for the experimental implementation and the subsequent data reduction.

Figure 1 depicts the imaging arrangement for these experiments. A dual-cavity, double-pulsing Nd:YAG laser (PIV-400, Spectra-Physics, with nominal output 400 mJ pulse^{-1} at 532 nm) serves as the light source. The pulse pairs are set to an inter-pulse spacing of 500 ns, and each image captures the scattering from both pulses in the pair. The 500 ns time spacing is well below the characteristic flow time scales. The laser pulses are formed into sheets with constant height that traverse the imaging area horizontally. We vary the laser sheet heights (over the range 3.5–5 cm) to match the sizes of the different imaging windows used (table 2), by using combinations of cylindrical lenses of nominal focal lengths 75 mm and 150 mm and spherical lenses of nominal focal lengths 550 mm and 670 mm. The sheet thicknesses at their focal

Window	Re_0	(x_{min}, x_{max})	(r_l, r_r)	Image size	N
I	1500, 2500	$(3.18d, 9.77d)$	$(4.44d, 4.39d)$	464×346	1000
II	800	$(7.89d, 14.59d)$	$(3.07d, 5.96d)$	464×346	1000
IIa	1500	$(7.89d, 14.51d)$	$(3.04d, 5.85d)$	464×346	1500
IIa	2500	$(7.89d, 14.51d)$	$(3.04d, 5.85d)$	464×346	1500
III	800	$(12.95d, 20.53d)$	$(2.16d, 8.02d)$	464×346	2000
IIIa	1500	$(12.84d, 20.61d)$	$(2.65d, 7.82d)$	348×260	2500
IIIa	2500	$(12.84d, 20.61d)$	$(2.65d, 7.82d)$	348×260	2500
IV	800	$(18.84d, 28.91d)$	$(3.22d, 10.26d)$	348×260	3000
IV	1500	$(18.84d, 28.91d)$	$(3.22d, 10.26d)$	348×260	3000
IV	2500	$(18.84d, 28.91d)$	$(3.22d, 10.26d)$	348×260	3000
V	800	$(25.25d, 38.04d)$	$(3.65d, 13.46d)$	348×260	3000
V	1500	$(25.25d, 38.04d)$	$(3.65d, 13.46d)$	348×260	3000
V	2500	$(25.25d, 38.04d)$	$(3.65d, 13.46d)$	348×260	3000

TABLE 2. Imaging window parameters for the experiments. The windows span from x_{min} to x_{max} downstream from the jet exit and extend to r_l and r_r on either side of the centreline. In the different windows the imaging array is binned to 464 columns by 346 rows or to 348×260. For a given jet exit Reynolds number Re_0 and a given imaging window, the data set includes N images.

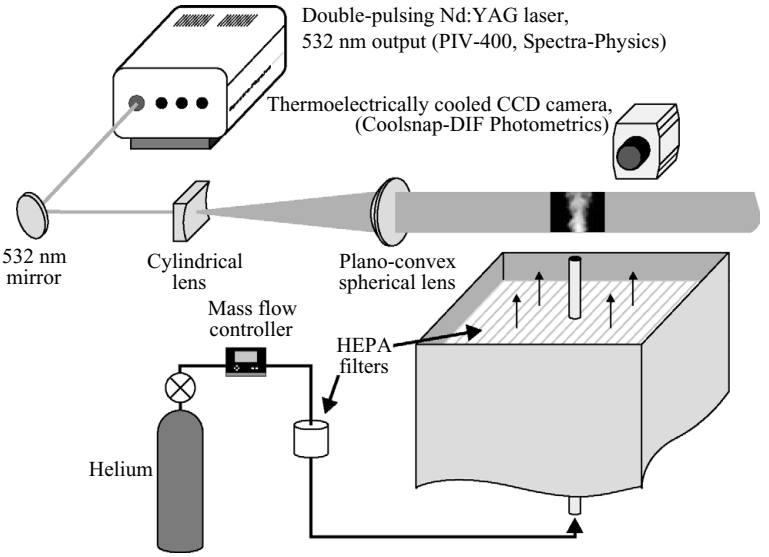

FIGURE 1. Schematic of the imaging arrangement.

point (which is placed on the jet centreline) is ≈200 μm, and the sheets generated by the two laser cavities are separated throughout the imaging region by no more than 20 μm. (Su & Clemens 1999 described the measurement method for sheet thicknesses and placement used here.) A thermoelectrically cooled CCD camera (Coolsnap HQ-DIF, Roper Scientific/Photometrics) captures the resulting Rayleigh scattering signal. Depending on the imaging window in question, the camera is fitted with a Canon FD 85 mm, or 50 mm, L-series lens operated at its full $f1.2$ aperture. Close-up lenses (+1 or +2 D, as needed) ensure proper focusing. The full camera resolution is 1392 × 1040 pixels, but the imaging array is binned (at either 3 × 3 or 4 × 4 pixels; table 2) to improve the signal-to-noise ratio.

Window	Re_0	Δx	$\lambda_{D,u}$, $\lambda_{D,d}$	$\Delta x/\lambda_{D,u}$, $\Delta x/\lambda_{D,d}$
I	1500, 2500	87.7 μm	–	–
II	800	89.7 μm	460 μm, 840 μm	0.20, 0.11
IIa	1500	88.3 μm	290 μm, 520 μm	0.30, 0.17
IIa	2500	88.3 μm	190 μm, 360 μm	0.46, 0.25
III	800	101.1 μm	750 μm, 1190 μm	0.13, 0.085
IIIa	1500	138.8 μm	460 μm, 750 μm	0.30, 0.19
IIIa	2500	138.8 μm	320 μm, 510 μm	0.43, 0.27
IV	800	178.7 μm	1090 μm, 1670 μm	0.16, 0.11
IV	1500	178.7 μm	680 μm, 1050 μm	0.26, 0.17
IV	2500	178.7 μm	470 μm, 710 μm	0.38, 0.25
V	800	226.8 μm	1460 μm, 2200 μm	0.16, 0.10
V	1500	226.8 μm	910 μm, 1380 μm	0.25, 0.16
V	2500	226.8 μm	620 μm, 940 μm	0.37, 0.24

TABLE 3. Spatial resolution parameters for the experiments. The pixel resolution in each imaging window is given by Δx. The estimated finest scale of scalar dissipative structures, in each window, is $\lambda_{D,u}$ at the upstream side of the window and $\lambda_{D,d}$ at the downstream side.

To avoid compromising spatial resolution, the full measurement region is covered by five individual imaging windows. Table 2 describes the locations and imaging parameters of these windows. The sizing of the imaging windows reflects the increasing size of the dissipative length scales with increasing x. Buch & Dahm (1998), for example, estimated the dissipative scale in the scalar field, λ_D, as

$$\lambda_D(x) = \Lambda_D\, \delta(x)\, Re_\delta^{-3/4}\, Sc^{-1/2}, \tag{2.8}$$

where $\delta(x)$ and Re_δ are as defined in § 2.1; $Sc \equiv \nu_\infty/D = 0.20$ is the Schmidt number (where D is the mass diffusivity of helium in air); and Λ_D is a proportionality constant. In (2.8), $\delta(x) \propto x$, while the remaining terms are constant; so the dissipation scale increases linearly with x. The resulting $\lambda_{D,u}$ at the upstream limit of each window, which is the minimum λ_D for the window and defines the most restrictive resolution condition, is shown in table 3, along with $\lambda_{D,d}$, the dissipation scale at the downstream limit of each window, and Δx, the pixel spacing in each window. The λ_D are computed using a conservative value of $\Lambda_D = 10$ in (2.8) (recommended values of up to $\Lambda_D \approx 15$ appear in the literature, e.g. Su & Clemens 2003). The spatial resolution of the measurements satisfies the Nyquist criterion throughout a given window if the relative measurement resolution $\Delta x/\lambda_{D,u} < 0.5$ for that window. Here, for $Re_0 = 800$, $\Delta x/\lambda_{D,u}$ is between 0.13 and 0.20; for $Re_0 = 1500$, it is in the range $0.25 < \Delta x/\lambda_{D,u} < 0.30$; and for $Re_0 = 2500$, it is in the range $0.37 < \Delta x/\lambda_{D,u} < 0.46$.

2.3. *Data reduction*

The low signal levels that characterize these negative scattering experiments place a significant burden of accuracy on the data reduction process through which the raw Rayleigh scattering images yield the helium mole fraction, X_{He}, by (2.7). Here, we implement a novel approach for measuring background light levels, in addition to accounting for non-uniform camera response efficiency, laser sheet attenuation and instantaneous, frame-to-frame variations in the local laser light intensity, I, across the imaging windows.

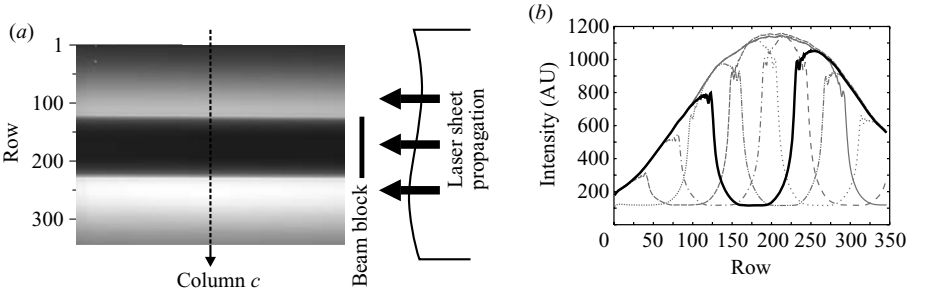

FIGURE 2. Measurement of background light levels. (*a*) An averaged image of scattering from ambient air only, with the partial beam block placed upstream of the imaging region as shown. (*b*) Cross-sheet scattering intensity profiles for different beam block positions, from column *c*, the centre column in the image in (*a*). The thick curve corresponds to the beam block position in (*a*). The background correction image is constructed column-by-column by interpolating/extrapolating on the minima of the different curves.

The raw imaging signal S at a given point can be decomposed as

$$S = (B) + [S_R] = (B_a + B_l) + [I \cdot E \cdot \sigma_m], \tag{2.9}$$

where the background signal B is any light captured by the imaging system that does not arise from laser Rayleigh scattering in the imaging plane, S_R, which is given in (2.6). The background signal itself has two components, namely B_l, which represents any uncontrolled diffuse or specular reflections that arise along the path of the laser pulses, and B_a, the contribution from ambient light and other light sources. In a well-controlled laboratory environment it is a simple matter to suppress non-essential light sources, rendering B_a negligible. However, the effect of the low signal levels in these experiments is to make B_l potentially of comparable magnitude to S_R.

The conventional approach to measuring background signal levels, which entails capturing images with the laser light source blocked prior to the measurement region, properly quantifies only the B_a component. The effect of uncontrolled laser reflections can originate anywhere along the laser path; so accurate measurement of B_l requires that the laser actually propagates through the measurement region. To allow this, while also preventing scattering from the imaging plane, we adopt a procedure in which we block a portion of the laser sheet prior to the measurement region. The shadow of the beam block then appears as a streak in the image. Since the majority of the sheet passes through the image, the resulting B_l closely reflects the actual measurement conditions, and B can be measured in the shadow of the block. The full B field is then constructed as the composite of a set of these streaks that cover the image plane. Figure 2(*a*) shows a sample average image from the background determination procedure. The laser sheet traverses the images from right to left throughout this paper. The bulk of the image shows the Rayleigh scattering from the ambient air, while the shadow of the beam block is evident as the dark streak. Figure 2(*b*) shows vertical, cross-sheet scattering intensity profiles, compiled across the centre column, for a set of eight different positions of the beam block. To construct the full B field, we proceed column-by-column, using profiles of the form in figure 2(*b*). On each column, the B profile is formed from linear interpolation/extrapolation on the locus of minimum points for the individual profiles.

The initial step in processing the data planes is to subtract this background field. Figure 3(*a*) shows a sample background-subtracted imaging field, S_R (2.6), from

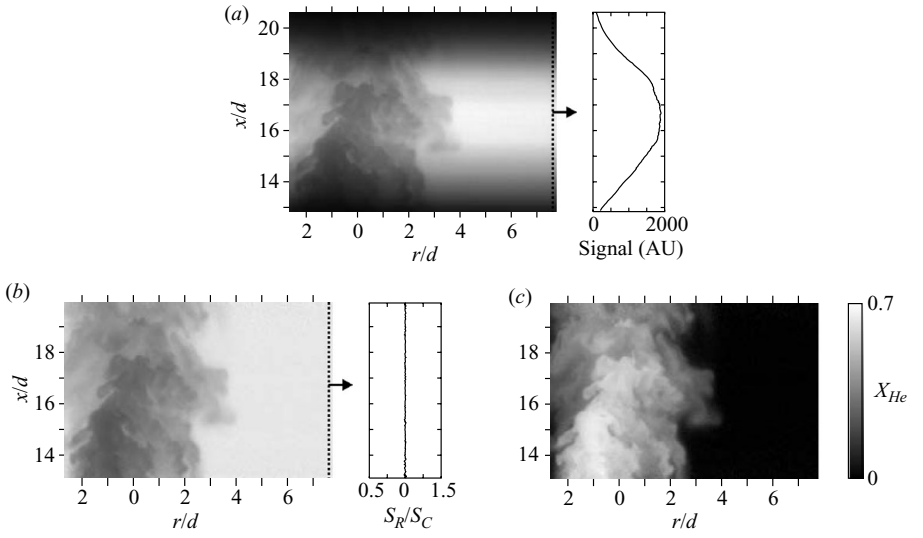

FIGURE 3. Stages in the data reduction process. (*a*) A sample imaging field from window III for the $Re_0 = 2500$ jet, after background subtraction to give S_R (2.6). The intensity profile corresponds to the dashed column indicated on the image. (*b*) The resulting S_F field, after sheet and response correction using the averaged correction field, S_c (2.10), and subsequent correction for the instantaneous laser sheet profile. (*c*) The resulting helium mole fraction field, determined using (2.7).

window III in the $Re_0 = 2500$ case. The signal in those regions of the image that contain only ambient fluid show clearly the spatial variation in laser sheet intensity, as indicated by the signal intensity profile shown. Subsequent to the background subtraction, we correct the data fields simultaneously for non-uniformity in the camera response (the E term in (2.9)) and variations in the laser sheet intensity, I, in an averaged sense. Camera response non-uniformity can arise, for example, through lens vignetting or pixel-to-pixel variations in the imaging array itself and can be assumed to be constant in time. Variations in I occur both in the cross-sheet direction (i.e. the vertical direction in figure 2), manifesting the spatial profile of the original laser pulse itself, and in the sheet propagation direction, as the result of spatial attenuation through scattering. The cross-sheet variations can fluctuate significantly in time, while the spatial attenuation is effectively constant. The correction field S_c for this step is measured as the (background-subtracted) Rayleigh scattering signal from ambient air only, giving

$$S_c = S_R(X_{He} = 1) = I \cdot E \cdot \sigma_{air}, \tag{2.10}$$

and variations in S_c are independent of composition. The background-subtracted data fields are then divided by this S_c to yield a tentative sheet- and response-corrected scattering intensity. By using the ambient air signal for the sheet correction, the corrected fields are equivalent to the scattering cross-section normalized by the air value.

It remains to correct the images further for instantaneous variations in the laser sheet intensity distribution. Each of the imaging windows employed here is specified so that the right side of the image contains ambient fluid only. At this stage of processing the signal levels in the ambient fluid should be identically 1; so any departure from that value represents deviation of the instantaneous sheet intensity

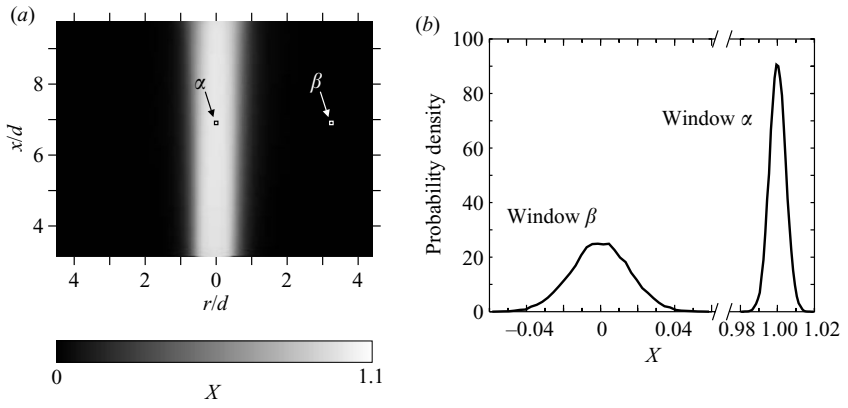

FIGURE 4. (*a*) The averaged helium mole fraction field from the near field of the $Re_0 = 800$ jet. (*b*) The probability density functions (p.d.f.s) of the helium mole fraction, X, from the windows labelled α and β in (*a*).

from the averaged intensity. We can then use the signal level profile in an arbitrary reference column from the ambient fluid region to correct the data in the remaining columns through column-by-column division, using knowledge of the laser sheet trajectory gleaned from the background measurements (figure 2*a*). In practice the effect of this correction is small; at any point in the field, the root mean square (r.m.s.) deviation of the instantaneous sheet intensity from the mean typically does not exceed 2 % of the maximum sheet intensity in the field. Figure 3(*b*) shows the final, corrected scattering image field S_F. Finally, figure 3(*c*) shows the resulting helium mole fraction, X_{He} (hereafter X), determined from the S_F field in figure 3(*b*) using (2.7).

2.4. *Signal quality*

The low signal levels characteristic of the present imaging arrangement make it important to quantify the noise levels of the measurements. Figure 4(*a*) shows the averaged X field from window I for the $Re_0 = 800$ jet (the signal-to-noise ratio here is not dependent on Re). In this region the flow is pre-transitional and essentially steady. We can obtain direct estimates of the noise levels in the helium mole fraction field by compiling X distributions in the two sub-windows indicated in the figure, namely window α located in the potential core and window β in the ambient air region. Figure 4(*b*) shows the probability distributions of X in windows α and β. The estimated signal–noise ratio is $\approx$227, based on the nominal maximum $X = 1$ and the signal standard deviation (0.0044) in the jet core (window α), and $\approx$64, based on $X = 1$ and the signal standard deviation (0.0157) in the ambient region (window β). The highest scattering signals, and thus the highest noise levels, occur in the ambient fluid region in these negative scattering experiments. In the remainder of this paper, the helium mole fraction results are processed with a 5×5 median filter to reduce noise levels with the least compromise in spatial resolution (Ghandhi 2006).

3. Results

3.1. *Mole fraction and fluctuation fields*

Figure 5 shows sample images of the helium mole fraction, X, for $Re_0 = 800$ and 2500. At $Re_0 = 800$ the flow is laminar for an extended region upon exiting the nozzle,

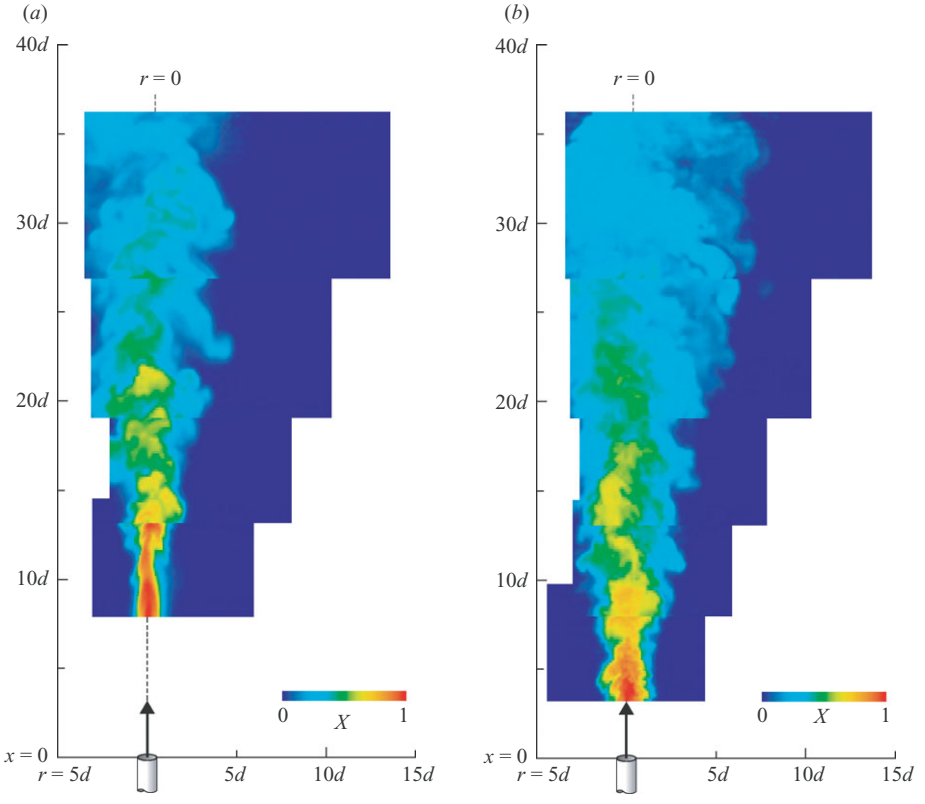

FIGURE 5. Sample helium mole fraction fields, X, for (a) $Re_0 = 800$ and (b) $Re_0 = 2500$.

so we will consider imaging measurements for windows II–V, omitting window I (the most upstream window). The instantaneous fields for the different windows are overlaid in the figure. For $Re_0 = 2500$, the flow is essentially turbulent from the outset, as is quite clear from the instantaneous X field window in window I. In the downstream windows, both Reynolds number cases are clearly turbulent. However, the higher-Re case contains manifestly smaller length scales, and its X field seems to be more uniformly distributed across the jet domain. At $Re_0 = 800$, the instantaneous images suggest that regions of pure ambient fluid may penetrate further towards the centreline than in the $Re_0 = 2500$ case. The distribution of pure ambient fluid has been considered by Dimotakis (2000) in the context of the turbulent mixing transition (and will be explored in additional detail in § 3.4).

Figure 6 shows the averaged helium mole fraction fields $\langle X \rangle$ for $Re_0 = 800$ and 2500. The averaging in each window is performed individually; so in particular there is no combined average computed in those regions in which imaging windows overlap. (In this way, figure 6 offers qualitative confirmation of the rigour of the data reduction process, in that the averaged X fields at the interfaces between windows are well matched, even though the image processing in each window is fully independent.) From inspection of these averaged fields, the turbulent transition for $Re_0 = 800$ appears to occur around $x/d = 10$, where the mole fraction field begins to spread. For $Re_0 = 2500$, the $\langle X \rangle$ field begins to spread upstream of window I.

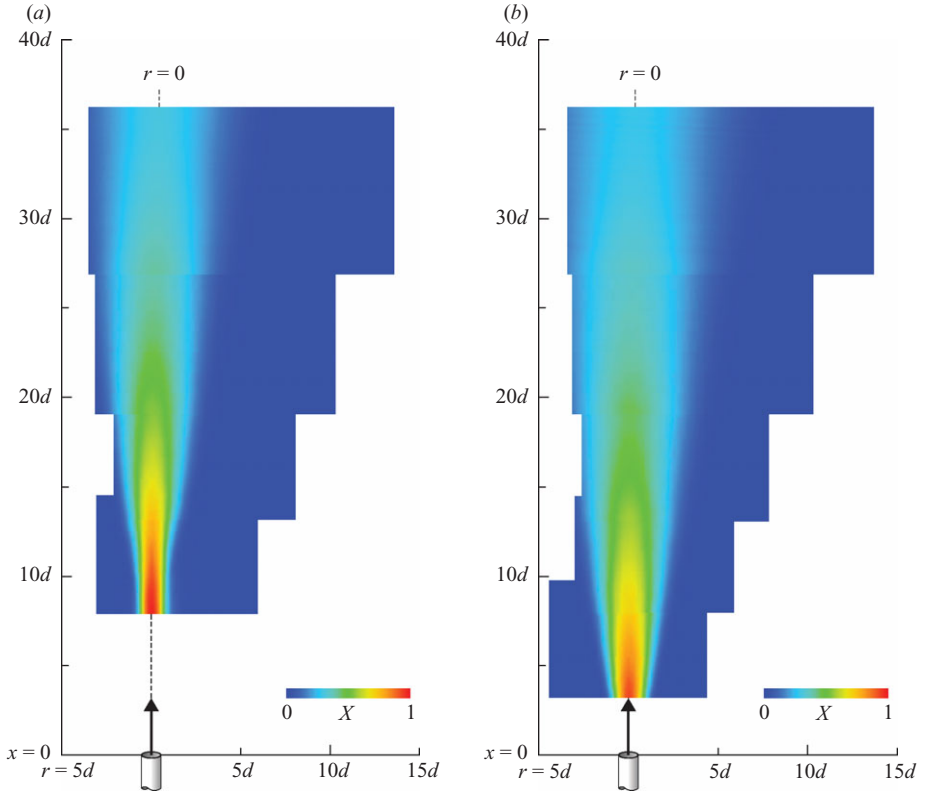

FIGURE 6. Averaged helium mole fraction fields, $\langle X \rangle$, for (*a*) $Re_0 = 800$ and (*b*) $Re_0 = 2500$.

The root-mean-squared helium mole fraction fluctuation fields, X'_{rms}, shown in figure 7, show the bimodal form that is characteristic of turbulent jets, in which peak fluctuations occur off the centreline (Townsend 1976). The X fluctuations originate in the jet shear layer, as the interface between the jet and ambient fluids becomes unsteady due to the initial shear layer instability. The zones of peak fluctuations then spread in tandem with the jet spread. The fluctuation fields in the $Re_0 = 800$ case confirm that the turbulent transition occurs around $x/d = 10$, as this is where the zones of peak X' originate. The peak fluctuation zones for $Re_0 = 2500$ originate upstream of the first imaging window, consistent with the jet spreading properties observed in the averaged X fields in figure 6. In comparison with the $\langle X \rangle$ fields in figure 6, the X'_{rms} fields in figure 7 are apparently not as well matched in the regions in which adjacent windows overlap, but as we will see in § 3.3, the matching between windows is more than adequate to provide a clear picture of the axial evolution of mean centreline fluctuations of both the mole and mass fractions.

3.2. *Similarity profiles*

Figure 8 shows radial profiles of the mean mole fraction, normalized by the individual profile maxima, for the three Reynolds numbers. For each downstream position x, the profiles are compiled from the mean mole fraction images by averaging the radial profiles for $x \pm 0.05d$. (All subsequent profiles are computed in a similar manner.) The profiles are shown in terms of the similarity coordinate $r/\delta_{0.5}$, where $\delta_{0.5}$ is the full width at half-maximum for each profile. For $Re_0 = 800$ (figure 8*a*), the most

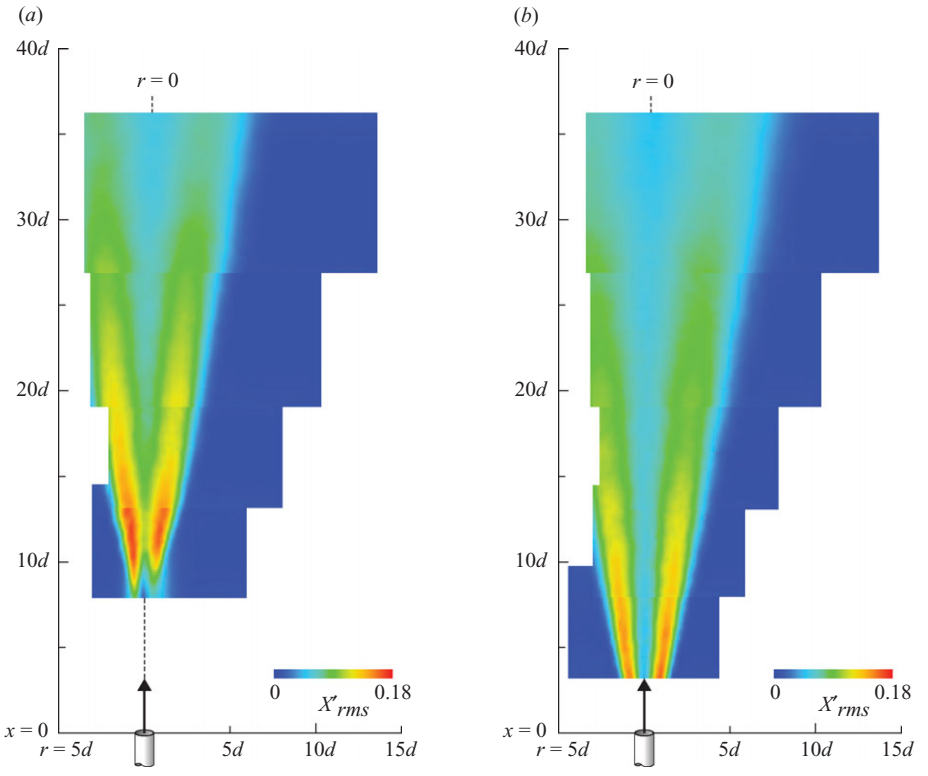

FIGURE 7. Root-mean-squared helium mole fraction fluctuations, X'_{rms}, for (*a*) $Re_0 = 800$ and (*b*) $Re_0 = 2500$.

upstream profile, from $x/d = 9$, is on average in the pre-transitional region (figure 6*a*), where molecular diffusion has a dominant role in establishing the mixing field; the form of the profile there is noticeably inconsistent with the other, turbulent profiles in that it is significantly wider. The turbulent profiles have a very consistent form. For $Re_0 = 2500$ (figure 8*c*), the flow is turbulent from the start of the measurement region; so the most upstream profile, from $x/d = 5$, does not show the particularly wide form seen in the $x/d = 9$ profile for $Re_0 = 800$. Instead, the $x/d = 5$ profile for $Re_0 = 2500$ is somewhat narrower than the downstream profiles, which probably reflects that the potential core is not closed in all cases at $x/d = 5$ (e.g. figure 6*b*). The turbulent advection would then be confined to a relatively narrow range on the jet outer boundary, consistent with a sharp X gradient and the observed narrow similarity profile. In this context, the consistency of the upstream, $x/d = 5$ profile for $Re_0 = 1500$ (figure 8*b*) with the downstream profiles reflects that the initial flow development is intermediate between the low-Re limit in which diffusion is dominant, leading to a wide $\langle X \rangle$ profile, and the high-Re limit, with its narrow near-nozzle $\langle X \rangle$ profile.

The consistency of the downstream profiles for each Re_0 suggests that each of the cases attains a reasonable level of self-similarity relatively early, no later than $x/d = 20$ for $Re_0 = 800$ and no later than $x/d = 15$ for $Re_0 = 1500$ and 2500. The similarity properties for $Re_0 = 800$ and 1500 do not appear to be affected by the presence of buoyancy; recall that these flows cross from the purely momentum-driven

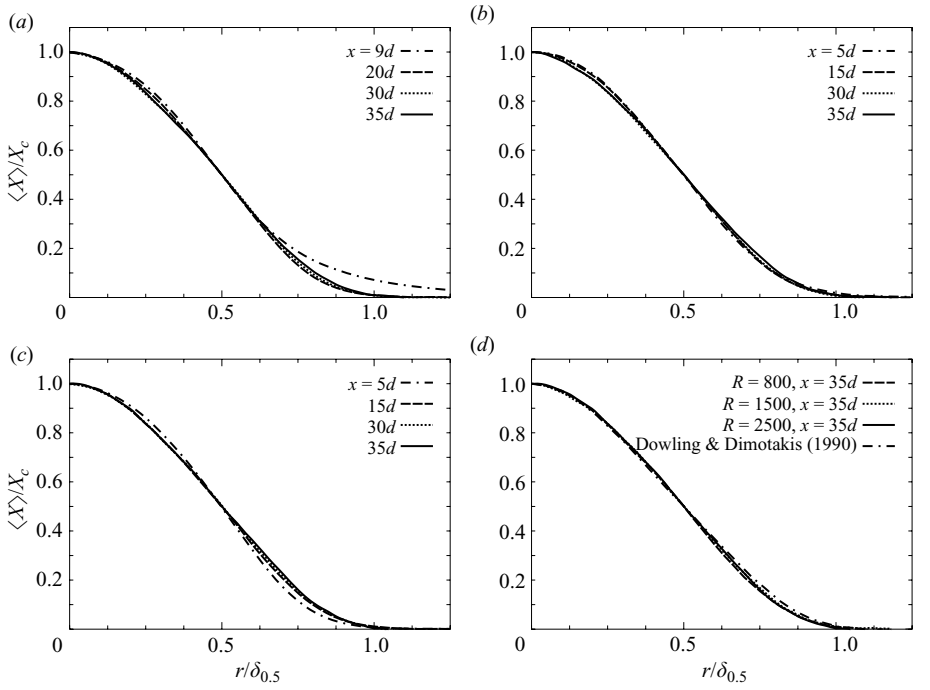

FIGURE 8. Normalized radial profiles of mean helium mole fraction for different x/d, presented in terms of the similarity coordinate $r/\delta_{0.5}$, for (*a*) $Re_0 = 800$, (*b*) $Re_0 = 1500$ and (*c*) $Re_0 = 2500$. Also shown is a comparison of the profiles at $x/d = 35$ for the different Re_0.

regime into the transitional regime within the range of the measurements (§ 2.1). George (1989) and Mi *et al.* (2001) have argued that self-similarity in jets may not be universal but instead depends on the details of the initial flow conditions. Figure 8(*d*) shows $\langle X\rangle$ profiles from $x/d = 35$, near the downstream limit of the measurements, for the three Re_0 values, together with the scalar similarity profile reported by Dowling & Dimotakis (1990) from single-point laser Rayleigh scattering measurements in constant-density axisymmetric jets. The present variable-density profiles are both consistent with each other and consistent with the Dowling & Dimotakis (1990) profile, most notably up to $r/\delta_{0.5} = 0.5$. At that point, the variable-density and constant-density profiles begin to diverge slightly, with the variable-density profiles having a more negative slope just beyond $r/\delta_{0.5} = 0.5$.

Figure 9 explores the discrepancy between the variable- and constant-density profiles by focusing on $r/\delta_{0.5}$ between 0.5 and 1. Also shown in the figure is the $\langle X\rangle$ profile measured in an ethylene–air (C_2H_4–air) jet at $Re_0 = 5000$, for which the density is nominally constant ($\rho_0/\rho_\infty = 0.97$) in the present flow facility. The ethylene–air system is a positive scattering system, with $\sigma_{C_2H_4} \approx 5.3\,\sigma_{air}$. The ethylene $\langle X\rangle$ profile is measured at $x/d = 25$ and is in the self-similarity region. The significant difference between the constant-density cases in the figure is that Dowling & Dimotakis (1990) employed a converging nozzle to obtain a near-uniform jet exit velocity profile, while the ethylene–air jet issues from a pipe. In the r range shown in figure 9, towards the outer boundary of the jet, the variable-density mole fraction profiles approach zero more rapidly than both constant-density profiles. This steeper profile slope, in regions in which the mean fluid composition predominantly consists of ambient fluid

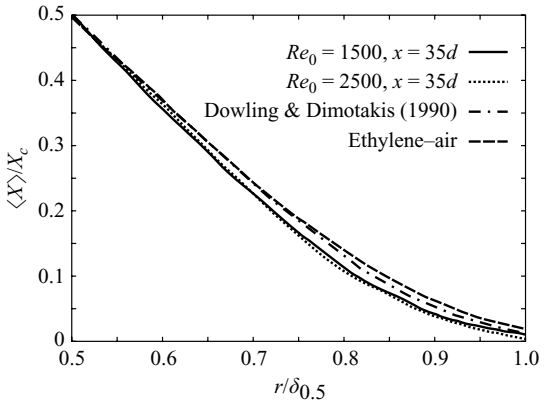

FIGURE 9. Comparison of the normalized mean helium mole fraction profiles at $x/d = 35$ for $Re_0 = 1500$ and 2500 with the constant-density profile measured by Dowling & Dimotakis (1990) and the profile measured in an ethylene–air jet in the present facility, focusing on the outer portion of the profiles.

(i.e. $X < 0.5$), means that the radial zone in which the helium jet fluid penetrates into the surrounding ambient fluid is relatively narrower for the variable-density jets. (We will revisit this point in conjunction with a discussion of the profiles of mean mass fractions.) There are discrepancies between the profiles from the constant-density cases, consistent with the hypothesis of George (1989) of the role of the initial flow conditions in establishing the self-similarity form, but the discrepancies do not affect the qualitative comparison between the variable- and constant-density cases.

Figure 10 shows the r.m.s. mole fraction fluctuation profiles for each Re_0 at different downstream locations. The profiles are normalized by $X'_{rms,c}(x)$, the local centreline r.m.s. fluctuations. For $Re_0 = 800$, the profiles vary only slightly for different x, but the differences are instructive. The widest X'_{rms} profile is just downstream from the turbulent transition ($x/d = 12$), consistent with the relatively broad $\langle X \rangle$ profile seen in the laminar region (figure 8*a*). By $x/d = 20$, this residual effect of the initial laminar profile is no longer evident, and the X'_{rms} profile width is consistent with those of the downstream profiles. However, the normalized peak fluctuation levels are evidently still evolving at $x/d = 20$. The onset of turbulence is manifest in the scalar fluctuations through the distortion of the jet–ambient fluid interface on the jet boundary, giving a sharp off-centreline peak in the X'_{rms} profile; as the flow moves downstream, and the effect of the turbulence is distributed across the width of the jet, the discrepancy between the peak X'_{rms} and the value on the centreline decreases. It appears that the X'_{rms} profile attains an approximately self-similar form by $x/d = 30$, with a peak fluctuation magnitude approximately 1.3 times the centreline value.

The r.m.s. fluctuation profiles for $Re_0 = 1500$ and 2500 also show clearly the evolution of the flow similarity. For both cases, the $x/d = 5$ profile has a peak X' magnitude over 2.5 times the centreline value. Again, by $x/d = 30$ this ratio of fluctuation magnitudes drops to an apparent asymptotic value of approximately 1.3. There is some evidence that the X'_{rms} profile shape continues to evolve, as the $x/d = 35$ profile may be slightly wider than the $x/d = 30$ profile, though this very small difference may simply reflect that these fluctuation measurements are very susceptible to experimental uncertainties.

We may also investigate the similarity of the mixing field in terms of the helium mass fraction, Y. Figure 11 shows normalized radial $\langle Y \rangle$ profiles for the three Reynolds

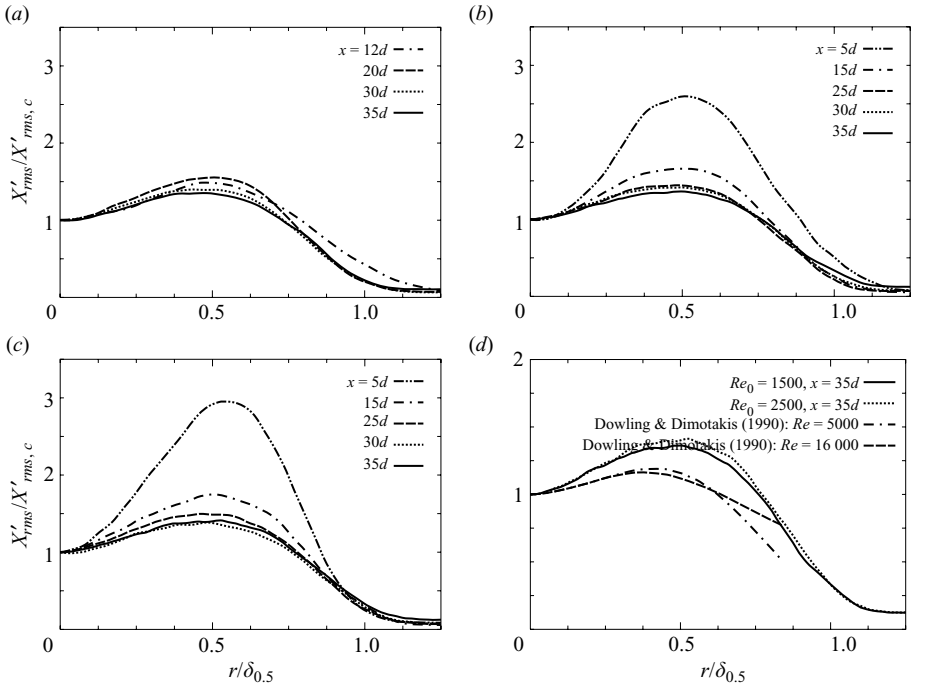

FIGURE 10. Normalized radial profiles of r.m.s. helium mole fraction fluctuations, X'_{rms}, for different x/d, presented in terms of the similarity coordinate $r/\delta_{0.5}$, for (*a*) $Re_0 = 800$, (*b*) $Re_0 = 1500$ and (*c*) $Re_0 = 2500$. (*d*) Comparisons of the $Re_0 = 1500$ and 2500 profiles at $x/d = 35$ with the profiles reported by Dowling & Dimotakis (1990) for $Re_0 = 5000$ and 16000. (Note the different vertical scale of *d*.)

numbers, where the r-coordinate is scaled with $\delta_{0.5,Y}$, the full width at half-maximum of these $\langle Y \rangle$ profiles. The determination of Y from the mole fraction is nonlinear; so there are differences between the $\langle Y \rangle$ profiles and the $\langle X \rangle$ profiles in figure 8. For example, the $\langle Y \rangle$ profile from $x/d = 5$ for $Re_0 = 2500$ is considerably wider than the downstream $\langle Y \rangle$ profiles, while the $\langle X \rangle$ profile from $x/d = 5$ for $Re_0 = 2500$ (figure 8*c*) is narrower than the downstream $\langle X \rangle$ profiles. The properties of the $\langle X \rangle$ profiles are perhaps more physically intuitive. For example, as mentioned above, the helium distribution in the near field at $Re_0 = 2500$ is essentially the initial top-hat profile with incipient turbulent transport on the edges, which is more consistent with the narrower form of the $\langle X \rangle$ profile rather than the wider $\langle Y \rangle$ profile.

As with the $\langle X \rangle$ profiles, the downstream $\langle Y \rangle$ profiles become self-similar. For the $\langle Y \rangle$ profiles this occurs by $x/d = 30$, slightly later than for the $\langle X \rangle$ profiles. Figure 11(*d*) shows the outer portion of the profiles for $Re_0 = 1500$ and 2500 at $x/d = 35$, compared with the constant-density profiles from Dowling & Dimotakis (1990) and the ethylene–air jet. The relation between the variable- and constant-density profiles differs from the relation for the mean mole fractions in figure 9. The outer parts of the variable-density profiles are in good agreement with the ethylene–air profile, consistent with the conclusion of Richards & Pitts (1993) that mass fraction profiles are similar for different density ratios. The slightly different form of the Dowling & Dimotakis (1990) profile, which approaches zero more quickly than the other profiles, would then be explainable by the differences in the initial jet profiles.

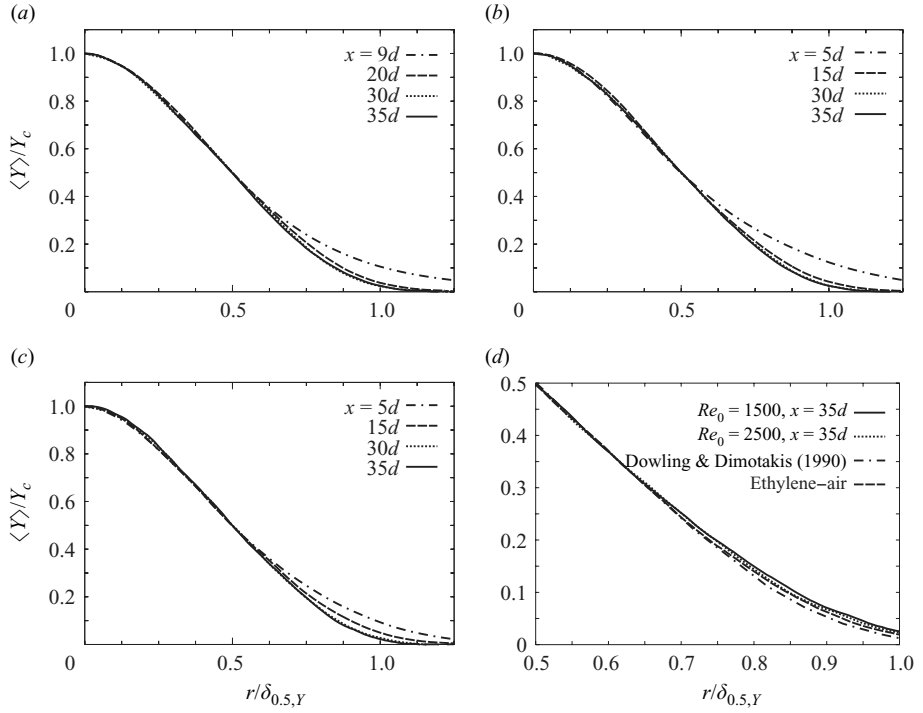

FIGURE 11. Normalized radial profiles of mean helium mass fraction for different x/d, presented in terms of the similarity coordinate $r/\delta_{0.5,Y}$, for (*a*) $Re_0 = 800$, (*b*) $Re_0 = 1500$ and (*c*) $Re_0 = 2500$. Also shown is a comparison of the outer portions of the $x/d = 35$ profiles with the constant-density profiles.

If the mass fraction similarity profiles are independent of the density ratio, we can explain the behaviour of the mole fraction profiles in figure 9 in terms of global entrainment relations. We first write $N_0 = m_0/MW_0$, where N_0 is the molar flow rate at the jet exit and MW_0 is the jet fluid molecular weight; similarly, $N_e(x) = m_e(x)/MW_\infty$, where $N_e(x)$ is the molar flow rate of entrained fluid, which has molecular weight MW_∞, at x. Then, the normalized molar entrainment N_e/N_0 is

$$\frac{N_e(x)}{N_0} = \frac{m_e(x)}{m_0}\frac{MW_0}{MW_\infty} = \frac{m_e(x)}{m_0}\frac{\rho_0}{\rho_\infty}, \tag{3.1}$$

where the latter equality is true because the present flows are isothermal. From (3.1) the normalized molar entrainment rates are decreased in light jets ($\rho_0 < \rho_\infty$) relative to the normalized mass entrainment m_e/m_0. This reduced molar entrainment explains the discrepancy between the helium mole fraction profiles and the constant-density profiles (figure 9). Further, in the present isothermal flow system, mole fractions correlate to volume fractions; so mixing as expressed in mole fractions can be interpreted in terms of the mixing of volume elements, which can in turn be interpreted directly in terms of turbulent transport and fluctuations. The $\langle X \rangle$ profiles in figure 9 thus suggest that the present low-density jets are characterized by reduced turbulent transport, which acts to mix the jet and ambient fluids, on the jet boundary, and that the magnitude of turbulent velocity fluctuations on the boundary is smaller for the low-density jets.

Figure 12 shows normalized profiles of Y'_{rms}, the r.m.s. fluctuations of the helium mass fraction. Again, certain trends differ from those seen in the X'_{rms} profiles in

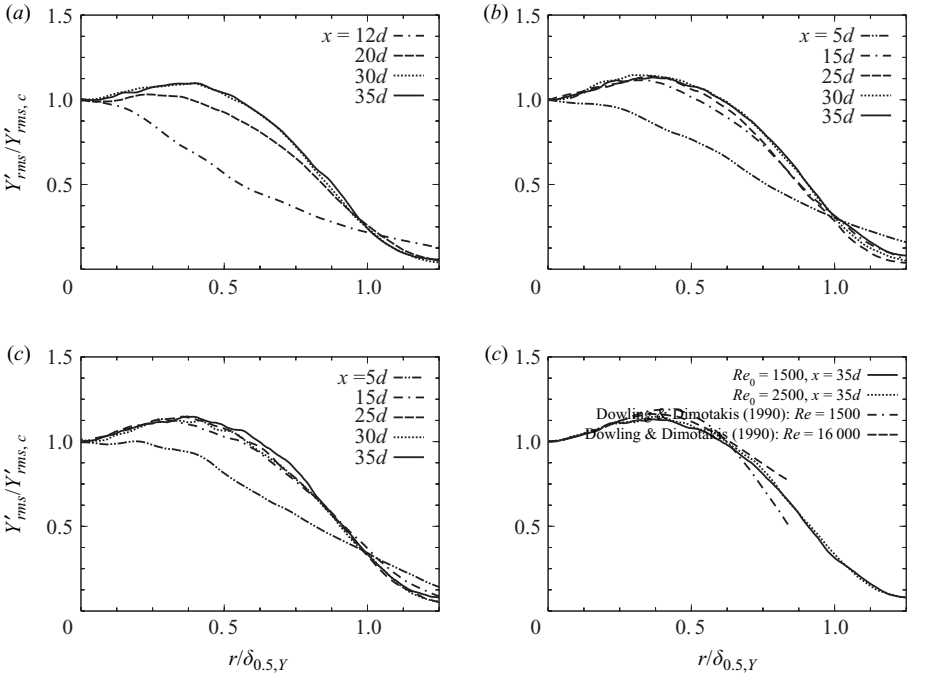

FIGURE 12. Normalized radial profiles of the r.m.s. helium mass fraction fluctuations, Y'_{rms}, for different x/d, presented in terms of the similarity coordinate $r/\delta_{0.5,Y}$, for (*a*) $Re_0 = 800$, (*b*) $Re_0 = 1500$ and (*c*) $Re_0 = 2500$. (*d*) Comparisons of the $Re_0 = 1500$ and 2500 profiles at $x/d = 35$ with the profiles reported by Dowling & Dimotakis (1990) for $Re_0 = 5000$ and 16 000.

figure 10. The near-field Y'_{rms} profiles are unimodal, having their maximum values on the jet centreline, with the characteristic bimodal form emerging downstream, while the X'_{rms} profiles in figure 10 are bimodal over the full axial measurement range, with the largest disparity between the peak values and centreline values occurring in the near field. Again, the properties of the mole fraction profiles are more consistent with the physical picture of turbulent mixing in the near field originating in the shear layer surrounding the jet, off the symmetry axis.

Even so, a comparison of figures 10(*d*) and 12(*d*) shows that the mass fraction fluctuation profiles for the buoyant jets are in better agreement with the constant-density jet results of Dowling & Dimotakis (1990) than are the mole fraction profiles, which is consistent with the hypothesis of Richards & Pitts (1993). In particular, the Y'_{rms} curves for $Re_0 = 1500$ and 2500 at $x/d = 35$ are in good agreement with the curve of Dowling & Dimotakis (1990) for $Re_0 = 16\,000$ for $r/\delta_{0.5,Y} \lesssim 0.6$, with a similar ratio of peak value to centreline value, beyond which the present curves lie between the $Re_0 = 5000$ and 16 000 curves from the earlier paper. We note that (table 1) the estimated outer-scale Reynolds numbers for the present $Re_0 = 1500$ and 2500 jets are $Re_\delta = 10\,100$ and 16 800, while the estimated Re_δ for the $Re_0 = 5000$ and 16 000 jets of Dowling & Dimotakis (1990) are 11 200 and 36 600. A notable difference between the present Y'_{rms} results and those of Dowling & Dimotakis (1990) is the absence of any discernible Reynolds number dependence in the present Y'_{rms} profiles. This may be because of the use of a contoured nozzle by Dowling & Dimotakis (1990) and a pipe nozzle in the present work. For sufficiently high flow rates pipe flow jet exit

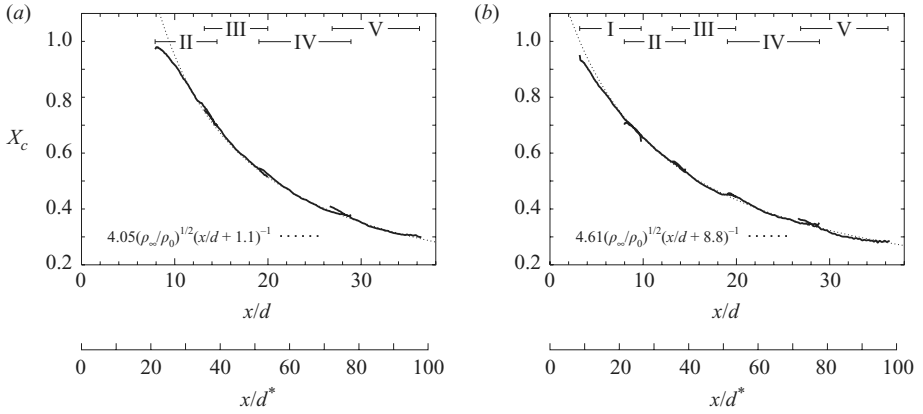

FIGURE 13. Axial evolution of the mean centreline helium mole fraction, $X_c(x)$, for (*a*) $Re_0 = 800$ and (*b*) $Re_0 = 2500$. The full axial extent of the measurements is composed of the individual curves for measurement windows I–V. The overall decay of X_c for each Re_0 is consistent with the x^{-1} pure jet scaling, as shown by the plotted curves $C(\rho_\infty/\rho_0)^{1/2}/(x-x_0)$, with scaling coefficients C and virtual origins x_0 determined through least squares fitting.

profiles will become independent of Re_0, while the boundary layer thicknesses in the contoured nozzle will continue to vary with Re_0 (Mi *et al.* 2001).

3.3. *Scaling properties*

The development of the mixing field in the jet can also be described in terms of the widths of the radial mean mole and mass fraction profiles and the scaling properties of the mean centreline mole and mass fraction values. Figure 13 shows the decay of the mean centreline mole fraction, X_c, as a function of the axial coordinate, x, for $Re_0 = 800$ and 2500. (In the remaining discussion the $Re_0 = 1500$ case is omitted for brevity.) For each Reynolds number, the X_c curve is determined individually for each imaging window, resulting in the overlapping curves in which the imaging windows coincide. The results for the three cases are all consistent with a jet-like, x^{-1} power decay of the centreline helium mole fraction. For each Reynolds number, the jet-like decay is represented in figure 13 by the curve $C(\rho_\infty/\rho_0)^{1/2}/((x-x_0)/d)$, where the scaling coefficient C and the virtual origin x_0 are determined through least squares fitting to the measured data. For $Re_0 = 800$, the least squares fit is performed in the range $x/d \in [20, 35]$, given $C = 4.05$, while for $Re_0 = 2500$ we used the data in the range $x/d \in [10, 35]$, giving $C = 4.61$. The virtual origin becomes progressively more negative with increasing Re_0 ($x_0 = -1.1d$ for $Re_0 = 800$, decreasing to $x_0 = -8.8d$ for $Re_0 = 2500$), consistent with a shortening of the potential core and a more rapid onset of turbulence.

Figure 14 shows the axial evolution of $\delta_{0.5}$, the full width at half-maximum of the mean X profile, for each Reynolds number. As with the centreline X decay curves in figure 13, $\delta_{0.5}$ is computed individually in each imaging window. The growth of the jet at each Re_0 is manifestly linear, as seen by the included lines $D(x-x_0)/d$, determined through least squares fitting. The axial ranges of the least squares fits are the same as those used for the centreline mole fraction fits above. The best fit coefficient $D = 0.19$ and 0.22 for $Re_0 = 800$ and 2500, respectively. The virtual origins x_0 differ slightly from those found previously by assuming jet-like decay of the centreline mole fractions (figure 13), though the trend of more negative x_0 with increasing Re_0 is again evident.

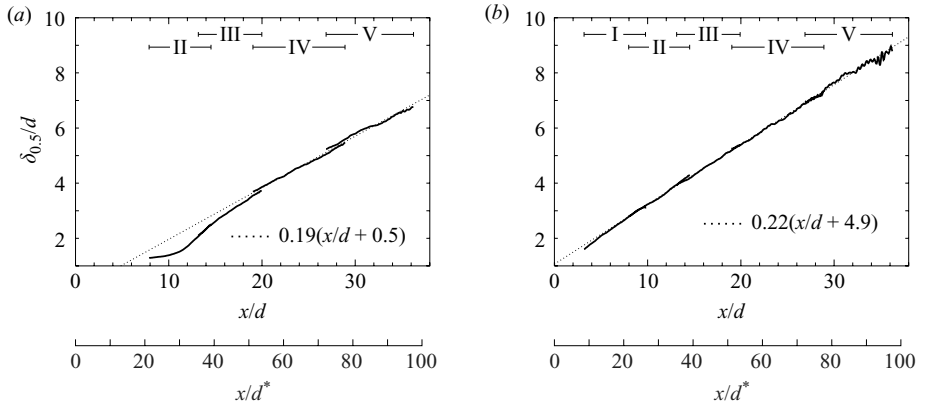

FIGURE 14. Axial evolution of the full width of the mean helium mole fraction profile at half-maximum, $\delta_{0.5}(x)$, for (*a*) $Re_0 = 800$ and (*b*) $Re_0 = 2500$. Also shown are the lines $D(x - x_0)/d$, with coefficients D and virtual origins x_0 determined through least squares fitting.

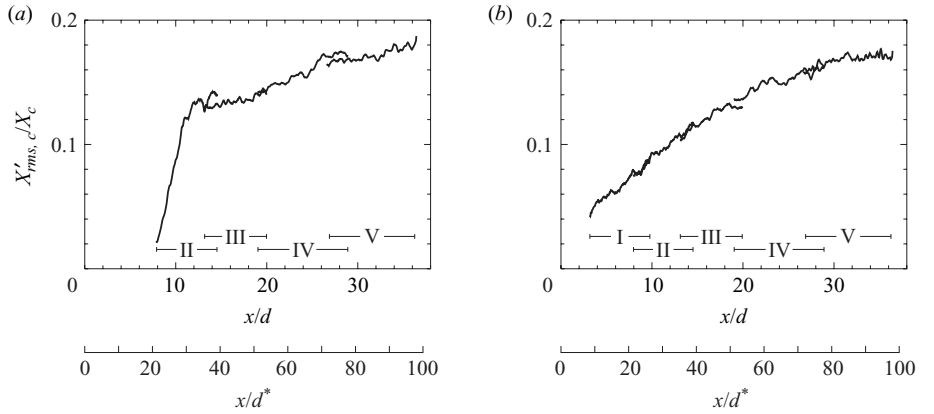

FIGURE 15. Axial evolution of the normalized r.m.s. helium mole fraction fluctuations on the centreline, $X'_{rms,c}/X_c$, for (*a*) $Re_0 = 800$ and (*b*) $Re_0 = 2500$. The $Re_0 = 2500$ jet appears to converge to a consistent fluctuation level of $\approx$18 % beyond $x/d = 30$.

The axial evolution of $X'_{rms,c}/X_c$, the normalized r.m.s. helium mole fraction fluctuations on the jet centreline, is shown in figure 15. For $Re_0 = 800$, $X'_{rms,c}/X_c$ increases monotonically through the downstream limit of the measurements, at which point $X'_{rms,c}/X_c \approx 0.18$. For $Re_0 = 2500$, it appears that the scaled fluctuations approach an asymptotic value of $X'_{rms,c}/X_c \approx 0.18$ for $x/d \gtrsim 30$ (or $x/d^* \gtrsim 80$).

Informative comparisons are available between the scaling properties of the helium mole and mass fractions. Figure 16 shows the axial evolution of $Y_c(x)$, the mean helium mass fraction on the centreline. As with the centreline mole fraction, Y_c observes a clear x^{-1} scaling. The least squares fits (for the same axial ranges as those used for the mole fraction analyses) to $C(\rho_\infty/\rho_0)^{1/2}/((x - x_0)/d)$ yield a coefficient $C = 0.565$ and virtual origin $x_0 = 8.7d$ for $Re_0 = 800$ and $C = 0.647$ and $x_0 = 2.1d$ for $Re_0 = 2500$. Relative to the decay curves for the centreline mole fraction in figure 13, the virtual origins are shifted in the positive x-direction, but as before the virtual origin for the $Re_0 = 2500$ case is to the negative-x side of that for the $Re_0 = 800$ case.

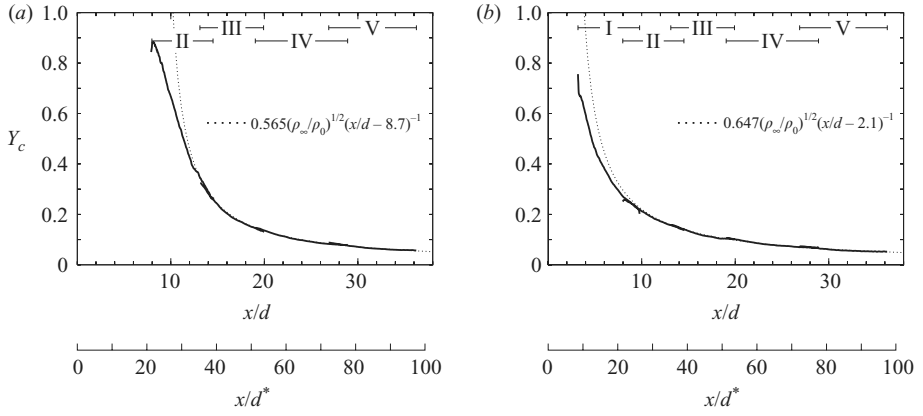

FIGURE 16. Axial evolution of the mean centreline helium mass fraction, $Y_c(x)$, for (a) $Re_0 = 800$ and (b) $Re_0 = 2500$. The full axial extent of the measurements is composed of the individual curves for measurement windows I–V. The overall decay of Y_c for each Re_0 is consistent with the x^{-1} pure jet scaling, as shown by the plotted curves $C(\rho_\infty/\rho_0)^{1/2}/((x-x_0)/d)$, with scaling coefficients C and virtual origins x_0 determined through least squares fitting.

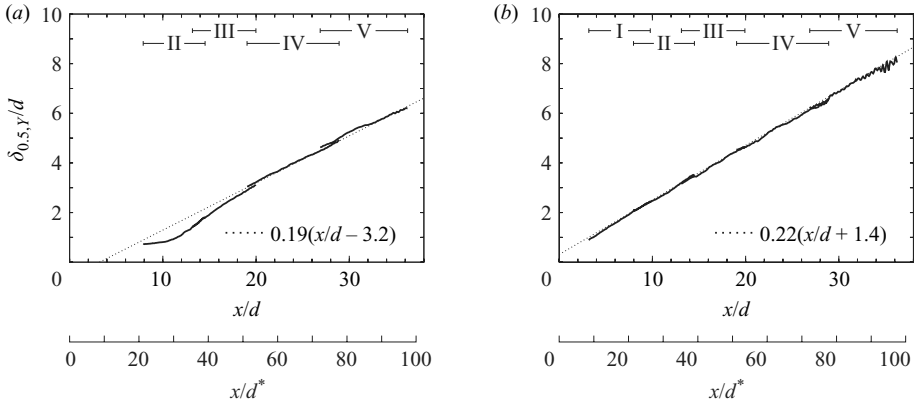

FIGURE 17. Axial evolution of the full width of the mean helium mass fraction profile at half-maximum, $\delta_{0.5,Y}(x)$, for (a) $Re_0 = 800$ and (b) $Re_0 = 2500$. Also shown are the lines $D(x-x_0)/d$, with coefficients D and virtual origins x_0 determined through least squares fitting.

Figure 17 shows the axial evolution of $\delta_{0.5,Y}(x)$, the full width at half-maximum of the mean radial mass fraction profiles. Again, $\delta_{0.5,Y}$ for $Re_0 = 800$ attains a linear dependence on x after the turbulent transition, while the linear growth of $\delta_{0.5,Y}$ is clear throughout the measurement domain for $Re_0 = 2500$. The least squares fits to $D(x-x_0)/d$ give $D = 0.19$ and $x_0 = 3.2d$ for $Re_0 = 800$ and $D = 0.22$ and $x_0 = -1.4d$ for $Re_0 = 2500$. The virtual origins for the flow width curves do not match exactly those for the centreline decay curves, though again the leftward shift of the virtual origin for higher Re_0 is intact.

Figure 18 shows the x-dependence of $Y'_{rms,c}/Y_c$, the scaled r.m.s. helium mass fraction fluctuation on the centreline. Here, unlike with the mole fraction fluctuations, the curves for $Re_0 = 800$ and 2500 both appear to achieve an asymptotic value within the measurement region ($x/d \gtrsim 30$ or $x/d^* \gtrsim 80$ for both values of Re_0), and the asymptotic value is apparently independent of Reynolds number, at $Y'_{rms,c}/Y_c \approx 0.23$.

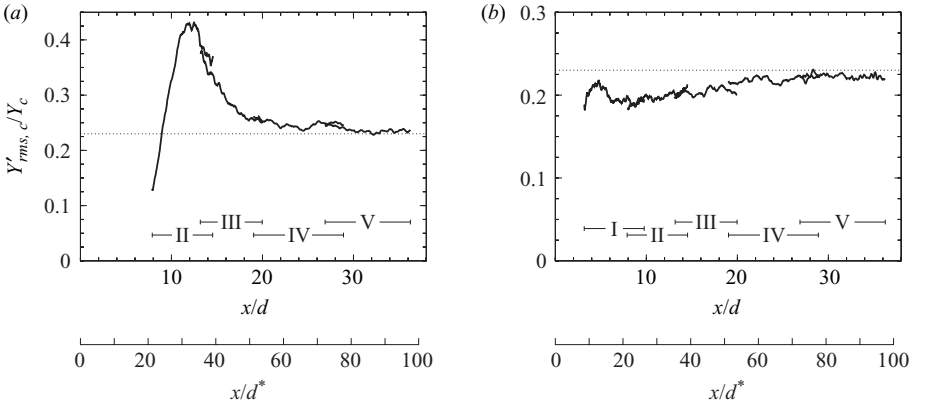

FIGURE 18. Axial evolution of the normalized r.m.s. helium mass fraction fluctuation on the centreline, $Y'_{rms,c}/Y_c$, for (*a*) $Re_0 = 800$ and (*b*) $Re_0 = 2500$. Both jet flows appear to converge to a consistent fluctuation level of $\approx 23\,\%$ (indicated by the dotted lines) beyond $x/d = 30$.

For the momentum-driven flow regime, Chen & Rodi (1980) recommended values for the scaling coefficients for the centreline decay, C (figures 13 and 16), and for the jet spreading rate, D (figures 14 and 17), of $C = 5.0$ and $D = 0.22$ (using the present definition of $\delta_{0.5}$ in terms of the full width). These recommendations are derived from compilations of previously reported measurements, for which the values of C range from 3.2 to 7 and those of D range from 0.17 to 0.26. Chen & Rodi (1980) defined their scalar variable in terms of the local density deficit relative to the ambient value, which relates directly to the helium mole fraction in these measurements; the C values found here for the centreline mole fractions, $C = 4.05$ and 4.61 respectively for $Re_0 = 800$ and 2500, are in good agreement with the values of Chen & Rodi (1980). The superior agreement for the higher Reynolds number may relate to the shortening of the laminar region as Re_0 increases. The scaling coefficient for the flow width, D, is similar for both the mole and mass-fraction-based definitions, at $D = 0.19$ for $Re_0 = 800$ and $D = 0.22$ for $Re_0 = 2500$, which again is in good agreement with the recommendation of Chen & Rodi (1980).

The observation that the asymptotic values of the the scaled mass fraction fluctuations are independent of the Reynolds number, while the scaled mole fraction fluctuations are not, suggests that the mass fraction is the more appropriate quantity for evaluating the similarity properties of the mixing field for variable-density jets. This is consistent with the earlier work of Pitts (1991*a*), who considered a range of jet-to-ambient density ratios ρ_0/ρ_∞. Pitts (1991*a*) found no consistency for the asymptotic mole fraction fluctuation values for ρ_0/ρ_∞ ranging from 0.14 (a helium jet, as in the present study) to 3.01 but identified a universal asymptotic value of the scaled mass fraction fluctuations of ≈ 0.23 for the different jets. The helium jet in that work was also momentum driven throughout the range of the measurements. Dowling & Dimotakis (1990) also measured scaled fluctuation magnitudes in their constant-density jets of ≈ 0.23 throughout their measurement region ($x/d \in [20, 90]$). The near universality of this fluctuation level apparently extends beyond the momentum-driven jet limit, as seen in the measurements of Panchapakesan & Lumley (1993), who reported scaled fluctuations between 0.21 and 0.22 in the region intermediate to the momentum- and buoyancy-driven regimes in their helium jets.

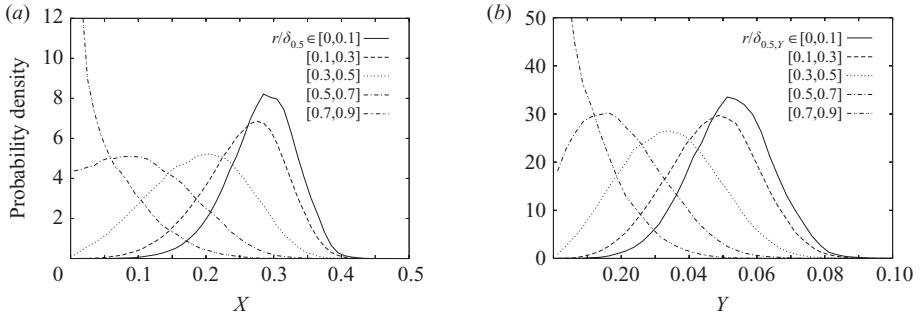

FIGURE 19. Probability distributions of (*a*) mole fractions and (*b*) mass fractions for the $Re_0 = 2500$ case, compiled for $x/d = 35 \pm 0.5$ and different ranges of the radial coordinate.

The very good agreement of the mole and mass fraction centreline decay, flow width and centreline fluctuation curves in figures 13–18 between the different imaging windows serves to confirm both the robustness of the data reduction process and the spatial resolution of the data. The data reduction to obtain the mole fractions in each imaging window is independent of the other windows; so in particular no overlap in the X_c or Y_c curves for the different windows is enforced. Meanwhile, the imaging windows are sized to maintain a roughly consistent relative resolution level (§ 2.2), but it remains that the relative resolution at the upstream and downstream sides of each window varies by a factor between 1.5 and 2 (table 3). In particular, the relative resolution of the downstream side of a given window is invariably superior to the resolution at the corresponding axial position on the upstream side of the next window. This resolution discrepancy is not evident in the $X'_{rms,c}$ curves, where the agreement in the window overlap regions is very good, suggesting that the spatial resolution is everywhere sufficient to measure the turbulent scalar fluctuations. We will see in § 3.6 that resolution disparities do noticeably affect the scalar fluctuations at worsened resolution levels.

3.4. *Scalar probability distributions*

Further insight into the structure of the mixing fields is available through the compilation of probability distributions of the helium mole and mass fractions in different regions of the flow. Figure 19 shows the probability density functions (p.d.f.s) X and Y from the $Re_0 = 2500$ jet compiled in six sub-windows, each with axial span $x/d = 35 \pm 0.5$ and with radial span $r/\delta \in [0, 0.1]$, $[0.1, 0.3]$, $[0.3, 0.5]$, $[0.5, 0.7]$ or $[0.7, 0.9]$, where δ is the local flow full width at half-maximum for either X or Y from § 3.3. At $x/d = 35$ both the mole and mass fraction fluctuation magnitudes appear to have converged to their asymptotic values (figures 15*b* and 18*b*); so the p.d.f.s in figure 19 should be representative of the full development of the mixing field. The mole and mass fraction p.d.f.s are very similar in form, with the most probable value in the distribution for each sub-window tracking with the local mean value, such that the most probable X and Y values decrease as the sub-windows move away from the centreline. The most noticeable difference between the X and Y p.d.f.s is that the mole fraction p.d.f.s for the different radial sub-windows have less homogeneous peak values and widths than the mass fraction p.d.f.s.

Figure 20 illustrates the axial evolution of these p.d.f.s for $Re_0 = 2500$, by showing the X and Y p.d.f.s compiled for $x/d = 10 \pm 0.5$, 15 ± 0.5, 25 ± 0.5 and 35 ± 0.5 and for radial ranges $r/\delta \in [0, 0.1]$, $[0.3, 0.5]$ and $[0.7, 0.9]$, normalized by the local

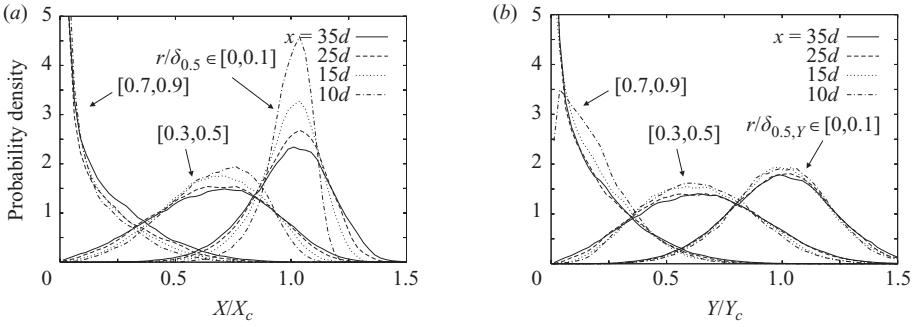

FIGURE 20. Probability distributions of (*a*) mole and (*b*) mass fractions, normalized by their local centreline average values (X_c and Y_c, respectively), for different axial and radial ranges in the $Re_0 = 2500$ jet.

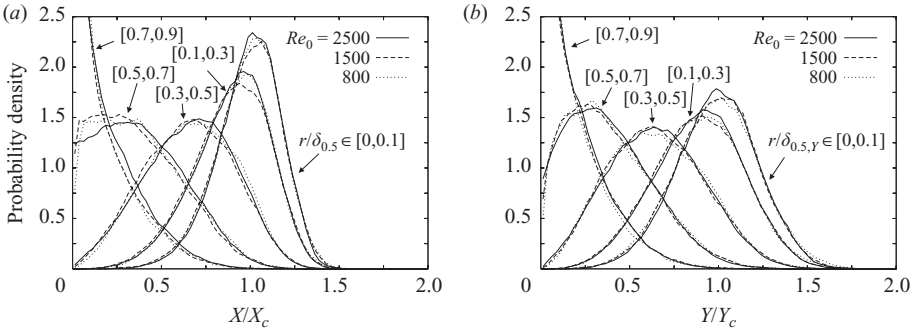

FIGURE 21. Probability distributions of (*a*) mole and (*b*) mass fractions for $Re_0 = 800$, 1500 and 2500, normalized by their local centreline average values (X_c and Y_c, respectively), compiled for $x/d = 35 \pm 0.5$ and different radial ranges.

centreline average values X_c or Y_c. The mole fraction p.d.f.s clearly evolve over the axial range of the measurements, particularly for the $r/\delta \epsilon [0, 0.1]$ sub-window that lies along the jet centreline. The mass fraction p.d.f.s, in contrast, are very consistent for the different x/d ranges. This relates directly to the more rapid convergence to their asymptotic values of the mass fraction fluctuations (figure 18) compared with the mole fraction fluctuations (figure 15).

The insensitivity of the mole and mass fraction p.d.f.s at $x/d = 35$ to the Reynolds number is illustrated in figure 21, which shows the mole and mass fraction p.d.f.s, normalized by their local centreline average values, in the same sub-windows as in figure 19. It is clear from the figure that the p.d.f.s in each sub-window for the different values of Re_0 are in very good agreement. The p.d.f.s in figure 21 also allow consideration of the argument put forth by Dimotakis (2000), who contended that pockets of ambient fluid could be found along the jet centreline for low Reynolds numbers but not for Reynolds numbers above a critical value that indicates the onset of the mixing transition. As indicated in § 2.1, the $Re_0 = 800$ jet here is expected to be short of the mixing transition, while the $Re_0 = 2500$ jet is expected to be in the neighbourhood of the mixing transition. However, the p.d.f.s in figure 21 are consistent with expected post-mixing transition behaviour for both $Re_0 = 800$ and 2500, in that there is a negligible likelihood of finding pure ambient fluid ($X = 0$ or $Y = 0$) in the sub-windows located along the jet centreline ($r/\delta \epsilon [0, 0.1]$). Focusing

specifically on the $X \rightarrow 0$ side of the normalized X p.d.f.s compiled for $r/\delta \epsilon [0, 0.1]$ (figure 21), we find that $X/X_c < 0.5$ for 0.79 % of the data points for $Re_0 = 800$, 1.05 % of the points for $Re_0 = 1500$ and 0.85 % of the points for $Re_0 = 2500$; so there is also no evidence that the likelihood of finding ambient fluid on the centreline decreases with increasing Re. We also note in figure 21 that the only distributions that have a local peak at $X = 0$ or $Y = 0$ are those that are compiled in the outermost sub-window ($r/\delta \epsilon [0.7, 0.9]$) for both Reynolds numbers. The absence of local peaks corresponding to ambient fluid towards the interior of the jet supports the argument that engulfment of ambient fluid at large scales is not the dominant entrainment process (Westerweel *et al.* 2005) and offers further evidence that the mixing at the Reynolds numbers shown in figure 21 is consistent with predicted post-mixing transition behaviour. Dimotakis (2000) pointed out that evidence for the mixing transition is particularly hard to detect in the turbulent jet and furthermore that for Schmidt numbers near unity, as for the present gas-phase jet, the effect of molecular diffusion can enhance the homogenization of the scalar field even for Reynolds numbers below the mixing transition. It is likely that the apparent similarity of the present concentration p.d.f.s, particularly those at lower Reynolds number, to the form anticipated to pertain beyond the mixing transition is because of to these Schmidt number effects.

3.5. *Scalar dissipation rates*

The proper scaling of χ, the scalar dissipation rate (1.1), in axisymmetric turbulent jets has resisted conclusive experimental verification. Peters & Williams (1983) estimated the scaling of χ by pursuing the analogy with the kinetic energy dissipation rate ϵ. Enforcing a balance of kinetic energy production at the large scales with dissipation at the small scales and applying classical scaling arguments for the velocity and flow width, the mean kinetic energy dissipation rate scaling on the centreline in axisymmetric jets is determined to be $\epsilon_c \propto x^{-4}$. Multiple experimental studies (e.g. Friehe, van Atta & Gibson 1971; Antonia, Satyaprakash & Hussain 1980) have confirmed this scaling of ϵ_c. Applying similar arguments, Peters & Williams (1983) moreover predicted that the mean centreline scalar dissipation rate goes as $\chi_c \propto x^{-4}$. Bilger (2004) explored the χ scaling through explicit consideration of the evolution equation for Y^2 and, assuming self-similarity and constant normalized centreline fluctuation levels, further found $\chi_c \propto x^{-4}$ for the axisymmetric jet.

However, numerous experimental studies have failed to confirm this scaling of the scalar dissipation rate. For example, Lockwood & Moneib (1980), using thermocouple probes, and Effelsberg & Peters (1988), using pointwise Rayleigh scattering, measured decay rates of χ_c that were noticeably slower than the expected x^{-4} in axisymmetric jets. Su & Clemens (1999), using imaging measurements in a planar jet, similarly measured a χ_c decay rate slower than the predictions of scaling arguments. Bilger (2004) has questioned the reliability of prior experimental studies of the scalar dissipation in jet flows, citing spatial resolution limitations. He has particularly cautioned against the use of dissipation scale estimates (e.g. λ_D (2.8)) alone to assess measurement resolution. Additionally, the measurements of Lockwood & Moneib (1980) and Effelsberg & Peters (1988) both used a fixed probe spacing over the full axial range of the χ measurements, and the measurements of Su & Clemens (1999) also employed a uniform imaging grid spacing. The relatively higher χ_c values in the downstream measurement regions, compared with the theoretical predictions, could indeed result from the increase in the dissipation length scales, and the commensurately less stringent resolution requirements, with increasing x. As

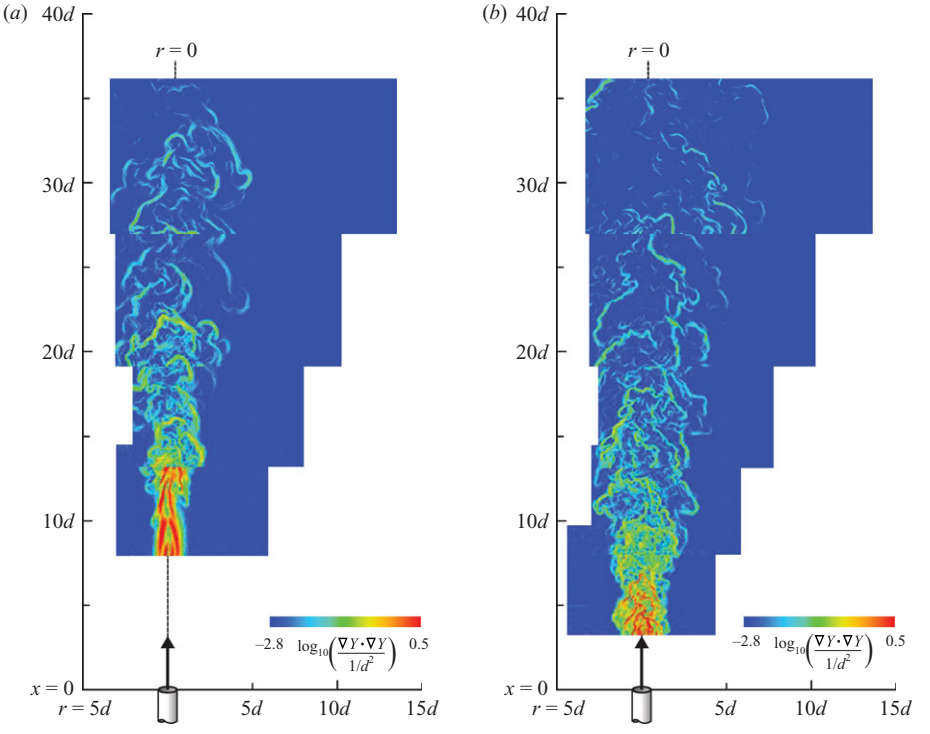

FIGURE 22. Two-dimensional, squared mass fraction gradient magnitudes, $(\partial Y/\partial x)^2+(\partial Y/\partial r)^2$, for (*a*) $Re_0 = 800$ and (*b*) $Re_0 = 2500$. Image planes correspond to those shown in figure 5.

described in § 2.2, the different imaging windows in the present measurements are sized to maintain a relatively consistent resolution over the full axial measurement range. We argued that these measurements are fully resolved in terms of λ_D in each of the measurement windows, but at the same time these measurements offer an additional check on resolution in the form of comparisons of the χ_c results between the different measurement windows.

From the present measurements we can perform spatial differentiation in the axial, x, and radial, r, flow directions to yield two components of the mass fraction gradient vector ∇Y which appears in the definition of χ (1.1). Figure 22 shows the two-dimensional, squared mass fraction gradient magnitudes, $(\partial Y/\partial x)^2 + (\partial Y/\partial r)^2$, for the same instantaneous image planes as those shown in figure 5. The gradient components are determined through two-point, second-order central differencing. There is a very wide range between the peak magnitudes in the near and far fields of the measurements, as seen by the logarithmic scaling of the colour map. The characteristic arrangement of high-gradient regions into a relatively sparse distribution of thin sheets that intersect the imaging plane as thin lines is clear (Buch & Dahm 1996, 1998), as is the tendency towards an $\approx 45^\circ$ inclination of these sheets to the streamwise direction in the relatively near-field range spanned by these measurements (Feikema, Everest & Driscoll 1996).

Multi-plane measurement methods have also been demonstrated that provide the full three-dimensional gradient vector, in both gas-phase and liquid-phase flows (Yip & Long 1986; Yip *et al.* 1987; Yip, Schmitt & Long 1988; Dahm, Southerland &

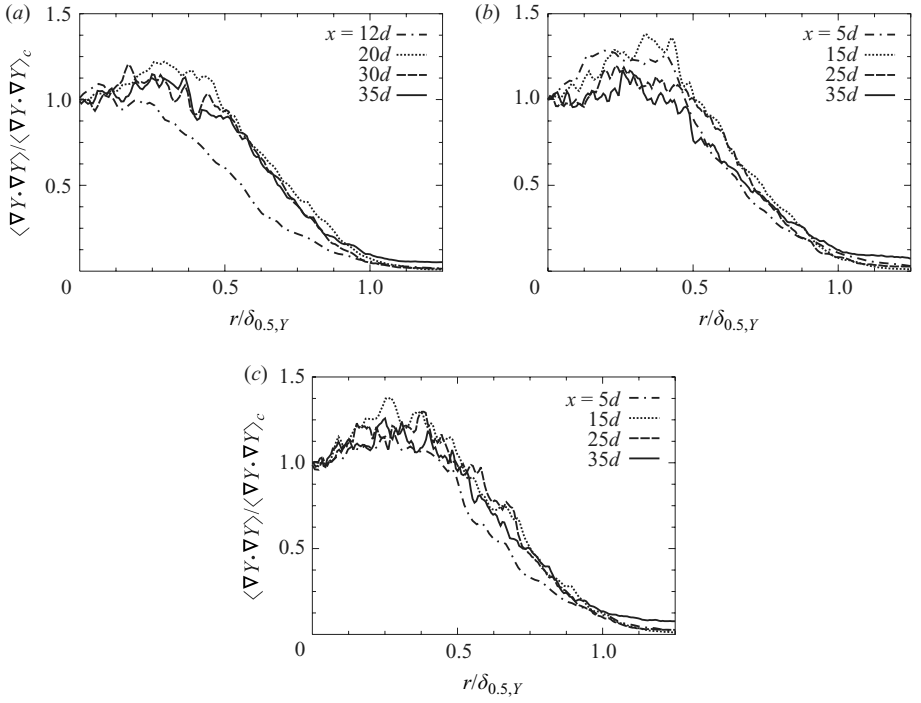

FIGURE 23. Normalized mean radial profiles of the estimated three-dimensional squared mass fraction gradient, $\langle(\partial Y/\partial x)^2+2(\partial Y/\partial r)^2\rangle$, for different x/d, presented in terms of the similarity coordinate $r/\delta_{0.5,Y}$, for (*a*) $Re_0 = 800$, (*b*) $Re_0 = 1500$ and (*c*) $Re_0 = 2500$.

Buch 1990; Su & Clemens 1999, 2003). With the present two-dimensional data we are confined to measurements of gradient components in the x–r plane; so to determine the scaling of the centreline mean scalar dissipation rate, χ_c, we will estimate the squared mass fraction gradient as

$$\langle \nabla Y \cdot \nabla Y \rangle = \left\langle \left(\frac{\partial Y}{\partial x}\right)^2 + \left(\frac{\partial Y}{\partial r}\right)^2 \left(\frac{1}{r}\frac{\partial Y}{\partial \theta}\right)^2 \right\rangle \approx \left\langle \left(\frac{\partial Y}{\partial x}\right)^2 + 2\left(\frac{\partial Y}{\partial r}\right)^2 \right\rangle, \qquad (3.2)$$

where the approximation represents the assumption of isotropy of the Y gradients in planes normal to the streamwise direction, x. This approximation becomes exact on the jet centreline, owing to the axial symmetry of the flow.

Figure 23 shows mean radial profiles of the estimated three-dimensional scalar dissipation, given by $\langle\chi\rangle \approx D\langle(\partial Y/\partial x)^2 + 2(\partial Y/\partial r)^2\rangle$, normalized by the centreline values. As with the X'_{rms} and Y'_{rms} profiles in figures 10 and 12, the asymptotic form of $\langle\chi\rangle$ has its peaks off the centreline. The peak values of the normalized $\langle\chi\rangle$ profiles are similar to the peak values of the normalized Y'_{rms} profiles, at 1.1–1.2. However, it appears that location of the peak $\langle\chi\rangle$ is slightly towards the jet centreline relative to the position of the peak Y'_{rms}.

The axial evolution of the mean squared Y gradient on the centreline, $\langle\nabla Y\cdot\nabla Y\rangle_c$, is shown in figure 24. Power-law scalings in these logarithmic axes manifest as straight lines; evidence for such scaling is very sensitive to any offset in the horizontal axes of the plots, and so the x-coordinates are offset by the virtual origins, x_0, determined from the least squares fits of the $1/x$ power law to the Y_c curves in figure 16. As with the foregoing results for the axial evolution of centreline concentrations, flow widths and

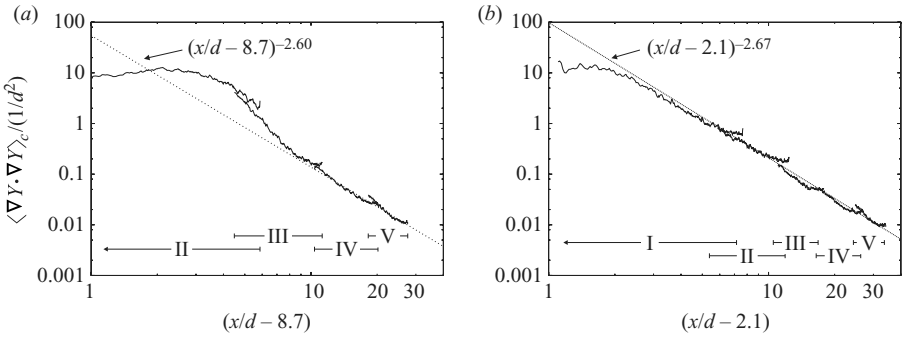

FIGURE 24. Axial evolution of the true mean squared mass fraction gradient on the centreline, $\langle \nabla Y \cdot \nabla Y \rangle_c$, for (*a*) $Re_0 = 800$ and (*b*) $Re_0 = 2500$, in log–log axes. The x-axis for each case is offset by the virtual origin, x_0, determined from the fit of the $1/x$ power law to the Y_c curves in figure 16. The squared Y gradients on the centreline decay as $x^{-2.6}$ for $Re_0 = 800$ and $x^{-2.67}$ for $Re_0 = 2500$.

centreline concentration fluctuations, the $\langle \nabla Y \cdot \nabla Y \rangle_c$ results in the different windows are in very good agreement with each other, which for these results points both to the accuracy of the data reduction and to the adequacy of the spatial resolution for the determination of the gradient terms.

Figure 24 also shows the best fit power-law curves for the $\langle \nabla Y \cdot \nabla Y \rangle_c$ results. These curves are determined from least squares linear fits to the logarithms of the data points, adjusted for the the respective virtual origins, and span the same x-ranges as used in § 3.3 for the fits to the Y_c curves. We find that $\langle \nabla Y \cdot \nabla Y \rangle_c$, and thus χ_c, goes as $x^{-2.60}$ and $x^{-2.67}$ for the $Re_0 = 800$ and 2500 jets. For the $Re_0 = 1500$ jet (for which $\langle \nabla Y \cdot \nabla Y \rangle_c$ is not shown here), $\chi_c \propto x^{-2.80}$. Similar to the earlier results in axisymmetric jets of Lockwood & Moneib (1980) and Effelsberg & Peters (1988), these measured decay rates are slower than the theoretical prediction, $\chi_c \propto x^{-4}$. Unlike those earlier studies, however, these measurements do not have the clear resolution compromise attendant to a fixed measurement grid spacing. In particular, there is no systematic reason for downstream χ_c values to be overestimated relative to the upstream values in these measurements. The density variations in the present measurements should also not affect the χ_c scaling, given that the other scaling properties examined in § 3.3 are all consistent with uniform-density jets.

It is possible, even given the attempted matching of the estimated spatial resolution levels between the different windows (table 3), that the resolution throughout the measurement range is insufficient to allow proper determination of χ_c and also that the resolution disparity across the span of each window is somehow too small to be manifest in mismatches of the χ_c curves in the regions of window overlap. However, as we shall see in the following section (in the discussion of figure 28), spatial under-resolution appears to increase, rather than decrease, the decay rate of χ_c. If indeed the proper decay rate of the centreline scalar dissipation is slower than the predicted $\chi_c \propto x^{-4}$, then it is worthwhile to consider where the discrepancy may arise. Bilger (2004) applied a number of simplifying assumptions in deriving the x^{-4} scaling, including the following: the mean velocity and scalar fields have self-similar radial profiles and follow classical jet scalings in the axial direction; the mean scalar r.m.s. fluctuation, Y'_{rms}, is self-similar, and its value on the jet centreline is proportional to the mean centreline scalar value, Y_c; the terms $\langle Y \rangle \langle u'Y' \rangle$ and $\langle u'Y'^2 \rangle$ involving axial turbulent fluxes, and the term $\langle D \nabla Y^2 \rangle$ involving molecular diffusion, are negligible

in comparison with $\langle u \rangle \langle Y^2 \rangle$ (where u is the axial velocity); and the radial profiles of $\langle \chi \rangle$ are self-similar. The agreement of the Y field with expected jet scaling has been demonstrated in § 3.3, and it seems safe to infer from that agreement that the velocity field, which is not measured here, also observes jet scaling. Meanwhile, figure 12 illustrates the self-similarity of Y'_{rms}, while figure 18 shows that Y'_{rms}/Y_c indeed approaches a constant value. In fact, Y'_{rms}/Y_c approaches its asymptotic value from above for $Re_0 = 800$ and from below for $Re_0 = 2500$, making it particularly unlikely that variations in the scalar fluctuation level account for the discrepancy between the measured and the predicted χ_c scaling. It is also unlikely that molecular diffusion effects can account for the observed discrepancy, because the measured power-law exponents are similar for the three Reynolds numbers considered here, which span from $Re_0 = 800$, for which the jet has an extended laminar region, to $Re_0 = 2500$, which is expected to be in the range of the mixing transition.

The present experiments provide less certainty regarding the validity of the other assumptions made in deriving the $\chi_c \propto x^{-4}$ scaling. For example, the absence of velocity field information precludes direct assessment of the magnitudes of the axial turbulent flux terms, while the radial $\langle \chi \rangle$ profiles in figure 23 are insufficiently converged to allow us to comment unequivocally on their self-similarity. One interesting observation that will be discussed in § 3.6 is that while the shapes of the radial profiles of the normalized Y' are not sensitive to spatial under-resolution, the shapes of the profiles of $\nabla Y \cdot \nabla Y$ are highly sensitive to the resolution level. It may be that the lack of similarity between the Y gradients measured at different spatial resolution levels is symptomatic of a general lack of self-similarity in the radial profiles of χ and that the failure of the present χ_c measurements to observe the predicted scaling properties is explained by the lack of the full development of the χ field. We must also note that the present two-dimensional measurements only provide an approximation of the full three-dimensional χ, but as mentioned before the centreline scaling measured using (3.2) is exact under the assumption of axisymmetry.

3.6. *Spatial filtering*

There is widespread current interest in the potential of the LES approach to compute practical flow systems, including combustion systems and atmospheric flows. Compared with DNS, LES achieves greater computational efficiency by computing the flows at a length scale (the 'grid' scale) that does not resolve the finest turbulent motions. The equations that describe the evolution of flow variables at the grid scale are determined by spatial filtering of the original evolution equations for fully resolved quantities; the effects of scales smaller than the grid scale are then entrusted to subgrid-scale (SGS) models. With an eye to eventual application in complex flow systems, numerous studies have considered the use of LES for relatively simple canonical flow systems like the turbulent jet. Validation of these LES results has employed highly resolved experimental data, in the same fashion as in the validation of DNS results, as well as using DNS results themselves. In particular, the *a posteriori* assessment of LES results proceeds by comparing computed quantities at the LES grid scales with the highly resolved data available from experiments or DNS.

However, LES results cannot strictly be evaluated in the same way as DNS results because LES results are, by definition, grid dependent (specifically regarding resolution) where true DNS results are not. This will not have a significant effect on the consideration of quantities, such as mean scalar concentration profiles, that are not particularly sensitive to resolution. However, quantities such as turbulent fluctuations, or spatial gradients, may be expected to be highly sensitive to resolution.

Re_0	Window	Filter A		Filter B		Filter C	
		Δ_A (pixel)	$\frac{\Delta_A}{\lambda_{D,u}}$, $\frac{\Delta_A}{\lambda_{D,d}}$	Δ_B (pixel)	$\frac{\Delta_B}{\lambda_{D,u}}$, $\frac{\Delta_B}{\lambda_{D,d}}$	Δ_C (pixel)	$\frac{\Delta_C}{\lambda_{D,u}}$, $\frac{\Delta_C}{\lambda_{D,d}}$
800	II	5	0.98, 0.53	15	2.9, 1.6	25	4.9, 2.7
	III	7	0.94, 0.59	22	3.0, 1.9	36	4.9, 3.1
	IV	6	0.98, 0.64	18	3.0, 1.9	30	4.9, 3.2
	V	6	0.93, 0.62	19	3.0, 2.0	32	5.0, 3.3
2500	IIa	5	2.3, 1.2	15	7.0, 3.7	25	11.6, 6.1
	IIIa	5	2.2, 1.4	16	6.9, 4.4	27	11.7, 7.3
	IV	6	2.3, 1.5	18	6.8, 4.5	31	11.8, 7.8
	V	6	2.2, 1.4	19	7.0, 4.6	32	11.7, 7.7

TABLE 4. Parameters for the simulated LES filtering. Filters A, B and C apply box filtering spanning $\Delta_i \times \Delta_i$ pixels in a given imaging window i. The resulting filtered resolution is expressed in terms of Δ_i/λ_D, where λ_D (as defined in (2.8)) is the estimated scalar dissipation scale at the upstream limit of each imaging window.

Validations of LES results for those quantities will ideally use experimental results with matched levels of resolution.

Planar imaging data are well suited for this purpose because they can be spatially filtered arbitrarily to any resolution level lower than that of the raw data. This spatial filtering is reflective of the filtering applied to derive the LES equations. Other work that has aimed to use experiments to measure filtered quantities for LES applications has focused on the details of SGS model specification and the *a priori* testing of model accuracy (e.g. Tong 2001; Wang & Tong 2002; Rajagopalan & Tong 2003; Su & Clemens 2003; Wang, Tong & Pope 2004). Here, we explore the effect of this simulated LES filtering on the mass fraction fluctuations and the scalar dissipation rates for the $Re_0 = 800$ and 2500 cases. Table 4 lists the parameters for the simulated LES filtering to obtain $\overline{Y}$, the filtered mass fraction field. We ignore window I here because the flow is not always turbulent in that window. For each window and each Re_0, we apply top-hat averaging filters (A, B and C) that represent successively lower resolution levels. The square filter kernels span $\Delta_i \times \Delta_i$, where, in window II, $\Delta_i = 5$, 15 and 25 pixels for filters A, B and C respectively. For the successive imaging windows, Δ_i for each of the three filters varies to match the relative resolution, as quantified by Δ/λ_D, at the upstream side of the different windows. For example, filter C in the $Re_0 = 2500$ case spans 25, 27, 31 and 32 pixels in windows IIa, IIIa, IV and V, giving relative resolution $\Delta_i/\lambda_{D,u} = 11.6$, 11.7, 11.8 and 11.7 at the upstream sides of those windows and $\Delta_i/\lambda_{D,d} = 6.1$, 7.3, 7.8 and 7.7 at the downstream sides. In order to represent LES filtering accurately, the filtering kernels do not overlap; so the grid spacing of the resulting filtered data is also given by Δ_i. Finally, the filtered grid for each window is aligned so that one grid cell in each (radial) row is centred on the flow centreline. For reference, we note that for the previously reported LES of round jets of Basu & Mansour (1999), Boersma (2004) and Suto *et al.* (2004), the relative resolution is $\Delta r/\lambda_D \approx 5$–7, where Δr is the computational grid spacing, and so the resolution levels represented here are characteristic of actual LES. (Strictly speaking, the relative resolution, Δ/λ_D, measures the degree to which a given grid fails to resolve the finest molecular mixing scale or, in LES, the departure from DNS resolution; it does not directly measure the ability of an LES grid to resolve the energy-containing flow scales.)

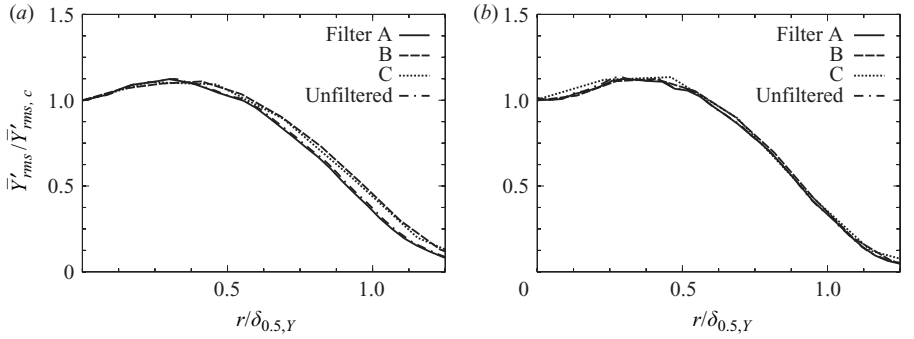

FIGURE 25. Radial profiles of $\overline{Y}'_{rms}$, the r.m.s. fluctuations of the filtered mass fractions, for the $Re_0 = 2500$ case, normalized by the values on the centreline, for filters A, B and C. Profiles from (*a*) $x = 15d$ and (*b*) $x = 30d$.

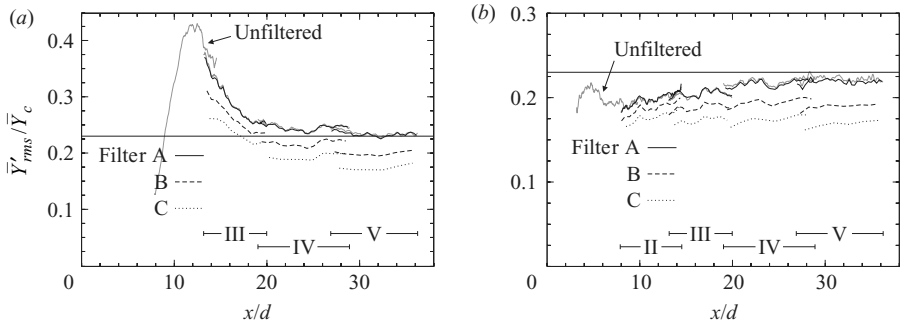

FIGURE 26. Axial evolution of $\overline{Y}'_{rms,c}/\overline{Y}_c$, the normalized centreline r.m.s. fluctuations for the filtered mass fraction fields, for (*a*) $Re_0 = 800$ and (*b*) $Re_0 = 2500$.

Figure 25 shows radial profiles of $\overline{Y}'_{rms}$, the r.m.s. fluctuations of the filtered mass fractions, for the $Re_0 = 2500$ case. The results for filters A, B and C are compared at $x = 15d$ and $x = 30d$. Each profile is normalized by its centreline value, $\overline{Y}'_{rms,c}$, and the radial coordinates are scaled with $\delta_{0.5,Y}$, the full width at half-maximum of the corresponding unfiltered profiles (figure 12). The shapes of the $\overline{Y}'_{rms}$ profiles have a small sensitivity to the spatial filtering, at the nearer-field location, $x = 15d$, while the $x = 30d$ profiles are essentially insensitive to the filtering. This slight discrepancy is perhaps explainable by figure 18(*b*), which shows that the jet appears to be in its asymptotic region (in terms of centreline Y fluctuation levels) at $x = 30d$ but not at $x = 15d$. It may be that the tendency towards relatively smaller fluctuation length scales towards the jet boundary, seen at $x = 15d$ in a heightened sensitivity to filter size (figure 25*a*), is a near-field artefact of the initial jet shear layer development and that a more uniform spatial distribution of fluctuation length scales is characteristic of the asymptotic region identified in figure 18(*b*). (Profiles of $\overline{Y}'_{rms}$ from the asymptotic regions of the $Re_0 = 800$ and 1500 jets, not shown here for brevity, are also insensitive to filtering, similar to figure 25.)

Figure 26 shows $\overline{Y}'_{rms,c}/\overline{Y}_c$, the normalized centreline r.m.s. fluctuations of the filtered mass fractions, for $Re_0 = 800$ (figure 26*a*) and 2500 (figure 26*b*). In comparison with the unfiltered fluctuations (repeated from figure 18), the fluctuation levels are essentially unchanged for filter A but are reduced by up to ~15 % for filter B

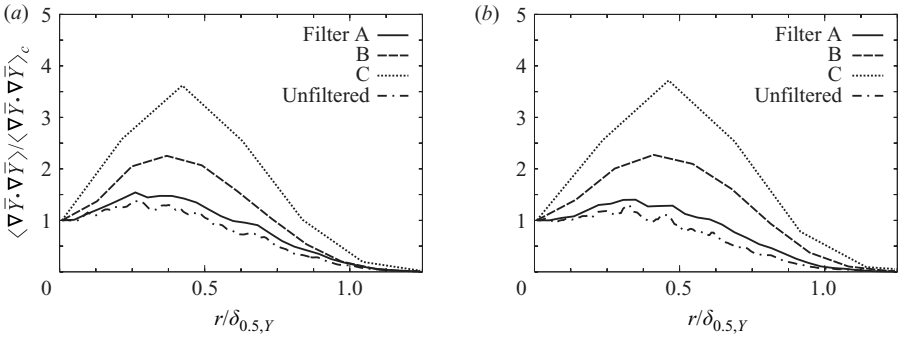

FIGURE 27. Normalized mean radial profiles of $(\partial\overline{Y}/\partial x)^2 + 2(\partial\overline{Y}/\partial r)^2$, the estimated squared three-dimensional gradient of the filtered mass fraction, for the $Re_0 = 2500$ case, for filters A, B and C. Profiles from (*a*) $x = 15d$ and (*b*) $x = 30d$. The profiles for the unfiltered mass fraction are shown for comparison.

and ~25 % for filter C. That is at grid spacing Δ_A the measured mass fraction fluctuations are still grid independent, while at Δ_B and Δ_C the fluctuations are in the grid-dependent regime, implying that the grid spacing Δ_A is adequate to resolve the turbulent mass fraction fluctuations, while Δ_B and Δ_C are inadequate. This is clear not only from comparing the $\overline{Y}'_{rms,c}/\overline{Y}_c$ magnitudes for the different filters within individual windows but also from comparing the $\overline{Y}'_{rms,c}/\overline{Y}_c$ magnitudes between windows. For filter A, the $\overline{Y}'_{rms,c}/\overline{Y}_c$ curves for adjacent windows overlap well, notwithstanding that the relative resolution in the overlap region of the adjacent windows differs (table 4). For filters B and C, the adjacent $\overline{Y}'_{rms,c}/\overline{Y}_c$ curves do not overlap. However, figure 26(*a*) shows that the curve for filter C in window III does overlap with the filter B curve in window IV, and a similar pattern is seen for the filter C/window IV and filter B/window V curves. This observation is consistent with the resolution estimates in table 4; for example, the relative resolution at the downstream side of window III for filter C is $\Delta_C/\lambda_{D,d} = 3.1$, while the relative resolution at the upstream side of window IV for filter B is $\Delta_B/\lambda_{D,u} = 3.0$. For $Re_0 = 2500$, the resolution estimates predict similar overlaps of the filter C curves in a given window with the filter B curves in the successive downstream windows, which is generally confirmed by the results in figure 26(*b*).

To examine the effect of spatial filtering on the measured scalar dissipation rates, figure 27 shows mean radial profiles of $(\partial\overline{Y}/\partial x)^2 + 2(\partial\overline{Y}/\partial r)^2$, the estimated squared three-dimensional gradient of $\overline{Y}$, for $Re_0 = 2500$, normalized by their centreline values and plotted against $r/\delta_{0.5,Y}$. Unlike the $\overline{Y}'_{rms}$ profiles, the mean $(\partial\overline{Y}/\partial x)^2 + 2(\partial\overline{Y}/\partial r)^2$ profiles are very sensitive to the filter size for both radial locations. The ratio of the peak mean squared gradient to the centreline value, which is ~1.1–1.2 for the unfiltered mass fractions, increases slightly for filter A, is in excess of 2 for filter B and is of the order of four for filter C. The radial position of the peak value may also be increasing with increasing filter size, but the small number of radial points for the larger filters makes it difficult to specify the position of the peak.

The discrepancy between the grid independence of the asymptotic $\overline{Y}'$ profiles in figure 25(*b*), and the grid dependence of the $\nabla\overline{Y}\cdot\nabla\overline{Y}$ profiles in figure 27, points to differences in the spatial distributions of the relevant length scales. As mentioned above, the insensitivity of the $\overline{Y}'$ profiles to the filter size suggests that the length

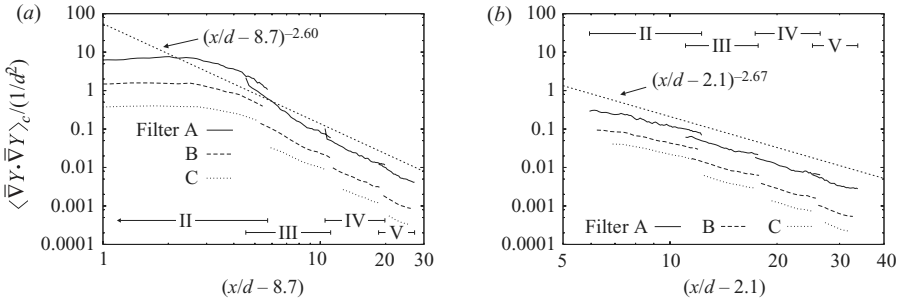

FIGURE 28. Axial evolution of $\langle \nabla \overline{Y} \cdot \nabla \overline{Y} \rangle_c$, the true squared three-dimensional gradient of the filtered mass fraction on the centreline, for (*a*) $Re_0 = 800$ and (*b*) $Re_0 = 2500$.

scales relevant to the scalar fluctuations are uniformly distributed across the radial span of the flow, so that the effect of a given filter is also uniform. In contrast, the length scales characteristic of scalar dissipation structures appear to be smaller towards the centreline of the jet, with the result that the spatial gradients there are reduced more noticeably with larger filter sizes. This non-uniformity of spatial scales does not appear to be the result of incomplete flow development in the axial direction, since the profiles for $Re_0 = 2500$ at $x = 15d$ and $30d$ are consistent with each other. The tendency of larger dissipation structures to occur at the outer boundary of the jet has previously been suggested by Pitts, Richards & Levenson (1999).

Figure 28 shows the axial evolution of $\langle \nabla \overline{Y} \cdot \nabla \overline{Y} \rangle_c$, the true squared three-dimensional gradient of the filtered mass fraction on the centreline, computed from the in-plane gradient components using (3.2), for $Re_0 = 800$ and 2500. The abscissas account for the virtual origins. The best fit power-law curves from the unfiltered results are shown for comparison. In contrast with the fluctuation results, the mean gradient magnitudes for $\overline{Y}$ are reduced relative to the results for Y even for filter A, suggesting that the grid spacing Δ_A is already inadequate to resolve the structures in the scalar dissipation rate field. The overlap between the curves in adjacent windows is slightly worse for filter A compared with the results for Y, while the power-law slope is not substantially changed. For filters B and C, the overlap between adjacent curves is notably worsened, and the results seem to indicate that the decay in the squared $\overline{Y}$ gradients becomes faster for the larger filter sizes. This last observation implies that the dissipation rate field is increasingly dominated by smaller spatial structures, which are more sensitive to spatial filtering, as the flow moves downstream. A possible explanation for this may be that in the near field, dissipation layers are more likely to exist at the interfaces between widely separated values of mass fraction, for example pure helium and pure air, which may tend to support thicker layers. That is while the length scale estimate $\lambda_D(x)$ may describe the smallest local dissipation layers or even the average size of the local dissipation layers, the mean squared mass fraction gradient (and thus the mean dissipation rate) may nevertheless reflect the presence of larger structures in the near field and the gradual reduction in the importance of those larger structures with increasing x.

The apparent increase in the decay rates for the squared gradient of the filtered mass fraction with increasing filter size, seen in figure 28, also suggests that the effect of under-resolution in measurements of the scalar dissipation rate would be to overestimate the exponent n in the power-law scaling $\chi_c \propto x^{-n}$. The discrepancy between the present estimate of $n \approx 2.7$ (figure 24) and the theoretical prediction

of $n = 4$ cannot then be explained by inadequate resolution. Section 3.5 previously enumerated possible physical explanations for this discrepancy.

The results in figures 26 and 28 make particularly clear that LES grid-scale results for scalar fluctuations and gradients must properly be validated by comparison with appropriately filtered experimental results. The fluctuation levels vary by up to 30 % for the range of the resolution levels considered here. The differences between the squared scalar gradients at different resolution levels are especially striking, given the logarithmic scale used in figure 28.

4. Conclusions

This work has demonstrated the application of planar Rayleigh scattering to quantitative measurements of mixing in axisymmetric turbulent helium jets issuing into air. The measurements span jet Reynolds numbers $Re_0 = 800$, 1500 and 2500, corresponding to estimated outer-scale Reynolds numbers $Re_\delta = 5400$, 10 100 and 16 800. The imaging region focuses on the relatively near field, up to 38 jet diameters downstream from the exit. In this measurement range the flows are momentum driven or at most have just entered the transitional range between being momentum or buoyancy driven. The sub-windows that cover the measurement region are sized to ensure spatial resolution sufficient for accurate determination of scalar fluctuations and scalar dissipation rates. The data reduction process pays special attention to corrections for background light levels and temporal and spatial variations in incident laser energy. The data reduction is sufficiently robust so that scaling quantities are consistently measured even across multiple imaging windows.

The mean jet fluid concentration fields, expressed in terms of either the mole fraction, X, or the mass fraction, Y, attain self-similarity within the measurement region, and jet-like scaling pertains for both the X and Y fields. The Y profiles are consistent with results from constant-density jets, in agreement with the earlier work of Richards & Pitts (1993). The X profiles, however, differ from constant-density profiles in a manner that can be explained by variations of molar entrainment rates with changes in jet-to-ambient fluid density ratios. The mole fraction results indicate a reduction in turbulent transport at the jet outer boundary for these low-density jets. Mass and mole fraction fluctuation profiles are also self-similar. Again, mass fraction fluctuation profiles and magnitudes are consistent with constant-density results, while the X' profiles and magnitudes are density dependent. The density dependence of the mole fraction results, which is particularly evident near the jet boundary, has implications for applications such as turbulent non-premixed combustion. It is well known that reaction zones in non-premixed jet flames tend towards the outer boundary of the jet, and flame stabilization in lifted flames appears also to be very sensitive to the details of the mixing in that region (e.g. Su *et al.* 2006).

The scalar dissipation rates show an axial decay rate slower than theoretical predictions for the jet. This is not probably the result of density variations in the present flow, given the agreement of the scaling properties of Y and Y' with the jet predictions; nor does the discrepancy appear to be due to resolution limitations, which have hampered prior experimental efforts to measure scalar dissipation rate scaling. From the present results, it seems more likely that the discrepancy with theoretical predictions is because of a lack of self-similarity of the present scalar dissipation rate profiles in the measurement region.

The two-dimensional extent of the measurements also allows spatial filtering similar to that inherent in LESs. The results confirm that fluctuation levels and scalar

dissipation rates determined for the filtered fields are reduced as the effective resolution is reduced, but while the fluctuation profiles for the filtered fields are similar for the different filter sizes, the forms of the scalar dissipation profiles are highly dependent on filter size. Experimental results such as these, which can be filtered to emulate varying levels of (under-)resolution, will be particularly useful for *a posteriori* assessments of LES results, by allowing for proper consideration of the grid dependence of LES results.

The authors thanks Mr James Barker for his assistance with the experiments and the reviewers for their valuable comments. This work is supported by the US National Science Foundation under grants CBET-0348208 and CBET-0534818.

REFERENCES

Antonia, R. A., Satyaprakash, B. R. & Hussain, A. K. M. F. 1980 Measurements of dissipation rate and some other characteristics of plane and turbulent jets. *Phys. Fluids* **23**, 695–699.

Bartels, J. *et al.* (Ed.) 1962 *Landolt–Börnstein Numerical Data and Functional Relationships in Science and Technology*, 6th edn. Springer.

Basu, A. J. & Mansour, N. N. 1999 Large eddy simulation of a forced round turbulent buoyant plume in neutral surroundings. In *CTR Annual Research Briefs* (ed. P. Moin & N. N. Mansour), pp. 239–248. Center for Turbulence Research.

Becker, H. A., Hottel, H. C. & Williams, G. C. 1967 The nozzle fluid concentration field of the round turbulent free jet. *J. Fluid Mech.* **30**, 285–303.

Bilger, R. W. 1976*a* The structure of diffusion flames. *Combust. Sci. Technol.* **13**, 155–170.

Bilger, R. W. 1976*b* Turbulent jet diffusion flames. *Prog. Energy Combust. Sci.* **1**, 87–109.

Bilger, R. W. 2004 Some aspects of scalar dissipation. *Flow Turbul. Combust.* **72**, 93–114.

Birch, A. D., Brown, D. R., Dodson, M. G. & Thomas, J. R. 1978 The turbulent concentration field of a methane jet. *J. Fluid Mech.* **88**, 431–449.

Boersma, B. J. 2004 Large eddy simulation of the sound field of a round turbulent jet. *Theoret. Comput. Fluid Dyn.* **19**, 161–170.

Buch, K. A. & Dahm, W. J. A. 1996 Experimental study of the fine-scale structure of conserved scalar mixing in turbulent shear flows. Part 1. $Sc \gg 1$. *J. Fluid Mech.* **317**, 21–71.

Buch, K. A. & Dahm, W. J. A. 1998 Experimental study of the fine-scale structure of conserved scalar mixing in turbulent shear flows. Part 2. $Sc \approx 1$. *J. Fluid Mech.* **364**, 1–29.

Chen, C. J. & Rodi, W. 1980 *Vertical Turbulent Buoyant Jets: A Review of Experimental Data*. Pergamon.

Dahm, W. J. A. & Dimotakis, P. E. 1987 Measurements of entrainment and mixing in turbulent jets. *AIAA J.* **25**, 1216–1223.

Dahm, W. J. A., Southerland, K. B. & Buch, K. A. 1990 Direct, high-resolution, four-dimensional measurements of the fine scale structure of $Sc \gg 1$ molecular mixing in turbulent flows. *Phys. Fluids* A **3**, 1115–1127.

Dimotakis, P. E. 2000 The mixing transition in turbulent flows. *J. Fluid Mech.* **409**, 69–98.

Dowling, D. R. & Dimotakis, P. E. 1990 Similarity of the concentration field of gas-phase turbulent jets. *J. Fluid Mech.* **218**, 109–141.

Eckbreth, A. 1988 *Laser Diagnostics for Combustion Temperature and Species*. Abacus.

Effelsberg, E. & Peters, N. 1988 Scalar dissipation rates in turbulent jets and jet diffusion flames. *Proc. Combust. Inst.* **22**, 693–700.

Escoda, M. C. & Long, M. B. 1983 Rayleigh scattering measurements of the gas concentration field in turbulent jets. *AIAA J.* **21**, 81–84.

Feikema, D. A., Everest, D. & Driscoll, J. F. 1996 Images of dissipation layers to quantify mixing within a turbulent jet. *AIAA J.* **34**, 2531–2538.

Friehe, C. A., van Atta, C. W. & Gibson, C. H. 1971 Jet turbulence: dissipation rate measurements and correlations. In *AGARD Turbulent Shear Flows, CP-93*, pp. 18-1–18-7.

George, W. K. 1989 Self-preservation of turbulent flows and its relation to initial conditions and coherent structures. In *Advances in Turbulence* (ed. W. K. George & R. Arndt), pp. 1–41. Springer.

Ghandhi, J. B. 2006 Spatial resolution and noise considerations in determining scalar dissipation rate from passive scalar image data. *Exp. Fluids* **40**, 577–588.

Leonard, B. 1979 Stable and accurate convective modelling procedure based on quadratic upstream interpolation. *Comp. Meth. Appl. Mech. Engng* **19**, 59–98.

Lockwood, F. C. & Moneib, H. A. 1980 Fluctuating temperature measurements in a heated round free jet. *Combust. Sci. Tech.* **22**, 63–81.

Mi, J., Nobes, D. S. & Nathan, G. J. 2001 Influence of jet exit conditions on the passive scalar field of an axisymmetric free jet. *J. Fluid Mech.* **432**, 91–125.

Nickels, T. B. & Perry, A. E. 1996 An experimental and theoretical study of the turbulent coflowing jet. *J. Fluid Mech.* **309**, 157–182.

Olsson, M. & Fuchs, L. 1996 Large eddy simulation of the proximal region of a spatially developing circular jet. *Phys. Fluids* **8**, 2125–2137.

Panchapakesan, N. R. & Lumley, J. L. 1993 Turbulence measurements in axisymmetric jets of air and helium. Part 2. Helium jet. *J. Fluid Mech.* **246**, 225–247.

Peters, N. & Williams, F. A. 1983 Liftoff characteristics of turbulent jet diffusion flames. *AIAA J.* **21**, 423–429.

Pitts, W. M. 1991*a* Effects of global density ratio on the centreline mixing behaviour of axisymmetric turbulent jets. *Exp. Fluids* **11**, 125–134.

Pitts, W. M. 1991*b* Reynolds number effects on the mixing behaviour of axisymmetric turbulent jets. *Exp. Fluids* **11**, 135–141.

Pitts, W. M., Richards, C. D. & Levenson, M. S. 1999 Large-and small-scale structures and their interactions in an axisymmetric jet. *Tech Rep.* NISTIR 6393. US National Institute of Standards and Technology.

Rajagopalan, A. G. & Tong, C. 2003 Experimental investigation of scalar-scalar-dissipation filtered joint density function and its transport equation. *Phys. Fluids* **15**, 227–244.

Richards, C. D. & Pitts, W. M. 1993 Global density effects on the self-preservation behaviour of turbulent free jets. *J. Fluid Mech.* **254**, 417–435.

Ricou, F. P. & Spalding, D. B. 1961 Measurements of entrainment by axisymmetrical turbulent jets. *J. Fluid Mech.* **11**, 21–32.

Su, L. K. & Clemens, N. T. 1999 Planar measurements of the full three-dimensional scalar dissipation rate in gas-phase turbulent flows. *Exp. Fluids* **27**, 507–521.

Su, L. K. & Clemens, N. T. 2003 The structure of fine-scale scalar mixing in gas-phase planar turbulent jets. *J. Fluid Mech.* **488**, 1–29.

Su, L. K., Sun, O. S. & Mungal, M. G. 2006 Experimental investigation of stabilization mechanisms in turbulent, lifted jet diffusion flames. *Combust. Flame* **144**, 494–512.

Suto, H., Matsubara, K., Kobayashi, M. & Kaneko, Y. 2004 Large-eddy simulation of flow and scalar transport in a round jet. *Heat Transfer Asian Res.* **33**, 175–188.

Tong, C. 2001 Measurements of conserved scalar filtered density function in a turbulent jet. *Phys. Fluids* **13**, 2923–2937.

Townsend, A. A. 1976 *The Structure of Turbulent Shear Flow*, 2nd edn. Cambridge University Press.

Wang, D. & Tong, C. 2002 Conditionally filtered scalar dissipation, scalar diffusion, and velocity in a turbulent jet. *Phys. Fluids* **14**, 2170–2185.

Wang, D., Tong, C. & Pope, S. B. 2004 Experimental study of velocity filtered joint density function for large eddy simulation. *Phys. Fluids* **16**, 3599–3613.

Westerweel, J., Fukushima, C., Pederson, J. M. & Hunt, J. C. R. 2005 Mechanics of the turbulent–nonturbulent interface of a jet. *Phys. Rev. Lett.* **95**, 174501.

Yip, B., Lam, J. K., Winter, M. & Long, M. B. 1987 Time resolved three-dimensional concentration measurements in a gas jet. *Science* **235**, 1209–1211.

Yip, B. & Long, M. B. 1986 Instantaneous planar measurement of the complete three-dimensional scalar gradient in a turbulent jet. *Opt. Lett.* **11**, 64–66.

Yip, B., Schmitt, R. L. & Long, M. B. 1988 Instantaneous three-dimensional concentration measurements in turbulent jets and flames. *Opt. Lett.* **13**, 96–98.

Zalesak, S. 1979 Fully multidimensional flux-corrected transport algorithms for fluids. *J. Comput. Phys.* **31**, 335–362.